wind

MDPI

Article

Multi-Model Assessment and Experimental Validation of a Custom High-Camber Airfoil for Wind-Lens Technology Application

Ayalew Bekele Demie [1,*], Venkata Ramayya Ancha [2,*] and Mulu Bayray Kahsay [3]

[1] Sustainable Energy Engineering Program, School of Mechanical Engineering, Jimma Institute of Technology, Jimma University, Jimma P.O. Box 378, Ethiopia
[2] JiT Center of Excellence, School of Mechanical Engineering, Jimma Institute of Technology, Jimma University, Jimma P.O. Box 378, Ethiopia
[3] Faculty of Mechanical and Industrial Engineering, Ethiopian Institute of Technology-Mekelle, Mekelle University, Mekelle P.O. Box 231, Ethiopia; mulu.bayray@mu.edu.et
* Correspondence: ayalew.bekele@ju.edu.et (A.B.D.); dra.venkata@ju.edu.et (V.R.A.)

Abstract

Diffusers in diffuser-augmented wind turbines (DAWTs) require high-camber airfoils operating at low Reynolds numbers (Re), and their laminar separation bubbles (LSB) significantly complicate aerodynamic predictions. No prior study has experimentally validated XFOIL, k-ω SST, and γ-Re_θ models against simultaneous lift, drag, and chordwise pressure coefficient (Cp) measurements for the customized high-camber airfoil at Re = 68,000 (68k), 118,000 (118k), and 159,000 (159k). Lift, drag, and Cp distributions were measured experimentally. The γ-Re_θ model demonstrated superior performance, achieving a lift maximum absolute percent error of 1.6–3.4%, near-zero bias, and a coefficient of determination >0.99. It accurately captured the LSB pressure plateau at mid-chord, with mean gross-averaged Cp percent errors of 8.1% and 2.1% for upper and lower surfaces, respectively. The k-ω SST model overpredicted lift by up to +9.8% at Re = 68k and underpredicted drag by up to 66%. XFOIL is unreliable specifically for separated transitional flows at Re < 118k, but improves at Re = 159k. The experimental dataset and validated transition-sensitive RANS approach provide a foundation for low-Re airfoil and DAWT diffuser design. Future work should extend measurements below Re = 50k and above 200k, including post-stall conditions, and system-level design of DAWT.

Keywords: diffuser-augmented wind turbine; low Reynolds number airfoil; laminar separation bubble; transition modeling; γ-Re_θ transition model; experimental validation; pressure coefficient distribution

Academic Editor: Firoz Alam

Received: 25 April 2026
Revised: 3 June 2026
Accepted: 5 June 2026
Published: 9 June 2026

1. Introduction

Conventional wind turbines exhibit inherent limitations in low-wind-speed regions, where complex flow patterns and size-related inefficiencies compromise economic viability [1,2]. Diffuser-augmented wind turbines (DAWTs) address these limitations by incorporating a duct that amplifies mass flow through the rotor [3–7]. The aerodynamic augmentation mechanism relies on the diffuser's profile to generate aerodynamic lift, lowering the downstream pressure and accelerating the local flow velocity immediately upstream of the rotor plane [8–11]. This localized increase in mass flow rate significantly enhances the kinetic energy available for extraction, leading to a substantially higher power output compared to an un-shrouded turbine of equivalent rotor diameter.

1.1. Airfoil-Shaped Diffusers

The diffuser shroud's cross-sectional geometry governs its flow acceleration capability. Early DAWT concepts employed simple conical or curved profiles that, while mitigating separation, generated minimal lift and modest power augmentation [12–16]. Airfoil-shaped cross-sections proved superior, uniquely combining internal flow acceleration along the pressure side with external suction along the suction side [11,17–19]. Engineered for high lift with minimal drag, airfoil sections have become the dominant geometry in modern DAWT research [20,21], making their selection and optimization fundamental to DAWT performance [4,22,23].

DAWT diffusers operate at low Reynolds numbers ($Re < 5 \times 10^5$), where airfoil aerodynamics are shaped by complex viscous phenomena [24,25]. Laminar boundary layers persist beyond maximum thickness, rendering them susceptible to adverse pressure gradients and separation [26,27]. The separated shear layer may transition and reattach, forming a laminar separation bubble (LSB) that alters pressure distributions and induces sudden changes in lift and drag [2,28]. Cambered airfoils are particularly sensitive to these effects: camber enhances lift but steepens the adverse pressure gradient on the suction side, promoting earlier separation and more pronounced LSB formation [16,29,30].

The Eppler E423 airfoil is well-documented for high-lift applications at low Reynolds numbers [19,31,32]. Wind tunnel studies show its performance is dominated by LSB behavior at lower Reynolds numbers. It represents high lift coefficient-achieving profiles, exceeding 1.5 at moderate angles of attack (10–15°) with favorable lift-to-drag ratios sustained up to 20–25° [21,33–35]. These attributes facilitate its ability to increase diffuser mass flow, making the E423 a promising candidate for DAWT applications. However, the sensitivity to flow conditions demands rigorous experimental validation of predictive models, as documented by previous studies [23,36].

1.2. Wind-Lens Technology: Principles, Performance Benefits, and Design Implications

The Wind-Lens represents a significant advancement in DAWT, distinguished by a compact ($L/D < 0.4$) geometric configuration that maximizes flow acceleration. As illustrated in Figure 1, the Wind-Lens consists of three primary components: an inlet shroud, a diffuser section with an airfoil-shaped cross-section, and a distinctive brimmed ring at the diffuser exit [37]. As the flow exits the shroud, the broad-ring brim induces vortex shedding, generating a deep, persistent low-pressure wake downstream. The resulting pressure differential draws a higher volume of air across the system, effectively magnifying the local velocity striking the rotor blades [38]. Consequently, this configuration yields a marked increase in the turbine's power generation capacity by optimizing the localized fluid velocity at the rotor plane.

The diffuser cross-section offers key aerodynamic advantages for Wind-Lens applications. The smoothly curved inlet reduces entry losses and ensures uniform flow at the rotor plane. The airfoil profile generates lift: the curved suction side creates a low-pressure region externally, while the pressure side creates a high-pressure region internally, drawing additional mass flow through the diffuser [37,38]. At low Reynolds numbers ($Re < 5 \times 10^5$), the smooth curvature delays flow separation by maintaining favorable pressure gradients, reducing drag, and preserving the pressure differential that drives flow acceleration.

Experimental studies demonstrate that Wind-Lens configurations generate between two and five times the power output of conventional bare turbines at identical rotor diameter and wind speed [37–39]. This augmentation factor enables economic viability in low-wind-speed regions. The performance of any WLT is fundamentally limited by its diffuser cross-sectional aerodynamics. The Eppler E423-derived airfoil examined in this study is specifically designed for this application. In our previous work [40], we performed

an aerodynamic optimization of the diffuser cross-section using CFD and Response Surface Methodology, which identified the E423-derived profile as a high-lift candidate for Wind-Lens technology operating at low Reynolds numbers. The present study extends that computational optimization by providing experimental benchmark data and multi-model validation for this airfoil.

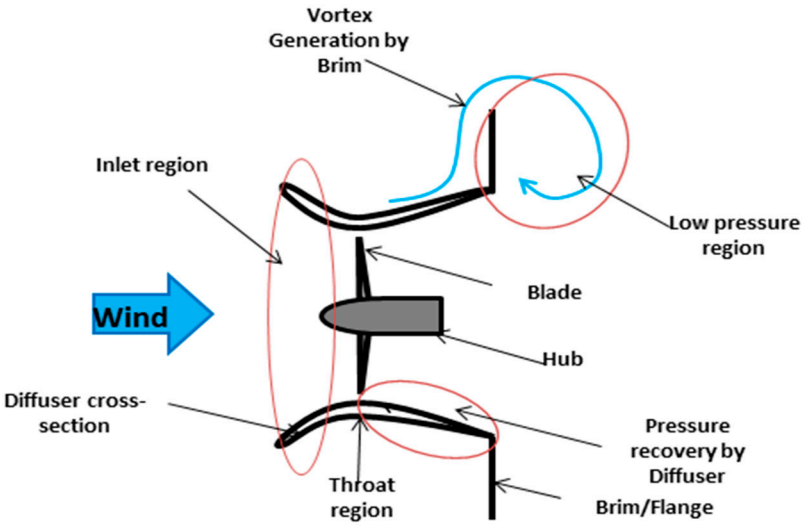

Figure 1. Schematic Diagram of Wind-Lens Technology.

1.3. The Need for Experimental Validation

The reliability of numerical results relies fundamentally on validation against experimental data. While computational methods such as RANS simulations and panel method codes like XFOIL offer efficient means for predicting airfoil performance, their accuracy cannot be relied on, particularly in complex flow regimes [20,41–43]. Therefore, validation serves as the critical bridge between numerical predictions and physical reality [44,45].

The importance of experimental validation is amplified in low-Reynolds-number flows because of the aerodynamic behavior governed by complex viscous phenomena, including LSBs and transition behaviors [24,25]. Turbulence models, even those calibrated for low-Re flows, can introduce significant uncertainty. Studies show that RANS simulations may overpredict lift and underpredict drag when transitional behavior is not accurately modeled [46–51]. Without validation against experimental data, these errors can remain and lead to optimistic performance predictions and suboptimal designs [23,38]. Studies documented that beyond model calibration, validation establishes an empirical foundation upon which improved models are built [2,28,52,53]. Advances in additive manufacturing now facilitate the production of high-fidelity models that precisely replicate computational geometries, which enables validation research that directly bridges computation and experiment [54–56].

1.4. Research Contribution and Objectives

This study is aimed at delivering a comprehensive experimental dataset for the E423-derived airfoil that was previously optimized using RSM-CFD in our own prior work [40], and systematically evaluating the predictive capabilities of three widely used modeling approaches for this custom E423-derived airfoil. The primary contribution of this work is generating a robust experimental dataset for the airfoil at three low Reynolds numbers (Re = 68k, 118k, and 159k) across angles of attack, AoA = 0–17.5°. Unlike the original CFD-only optimization, these datasets are lift and drag coefficients, surface pressure measurements for chord-wise Cp distributions on both upper and lower surfaces, and comprehensive uncertainty quantification to establish quality.

Building upon this experimental foundation, the study performs multi-model (γ-Re_θ, the k-ω SST, and the XFOIL) validation in which the predictive models span different fidelity levels. These models are systematically assessed against the experimental data. Model accuracy is quantified using comprehensive statistical metrics, including mean absolute error (MAE), root mean square error (RMSE), bias, maximum local error, Pearson correlation coefficient (r), and coefficient of determination (R^2). These metrics are applied to lift and drag coefficients across all angles of attack, pressure coefficient distributions resolved by chord position, and sensitivity analyses with respect to Reynolds number and angle of attack.

The final contribution of this work lies in translating the validation outcomes into practical modeling guidelines for DAWT diffuser design. By identifying the strengths and limitations of each modeling approach across transitional and fully turbulent flow regimes, this study provides designers with evidence-based recommendations for selecting appropriate methods based on their specific operating conditions and design requirements.

Through the multi-model validation of widely used design tools against experimental data for our previously CFD-optimized profile [40], the present work establishes a credible foundation for their application in developing efficient low-Re airfoil customization. This experimental dataset serves as the first validation of our own RSM-CFD-optimized design, and the data generated herein serve as a reference for future model development and validation efforts, contributing to improved DAWT performance in low-wind-speed regions.

2. Materials and Methods

This study presents the generation of experimental aerodynamic data and the validation of computational models for a custom airfoil specifically optimized for the diffuser cross-section of a DAWT. The airfoil geometry was derived from the Eppler E423 (Profiles program, Richard Eppler, Universität Stuttgart, Germany) profile and optimized using a combined CFD-based Response Surface Methodology (RSM) framework that incorporated XFOIL (Mark Drela, Massachusetts Institute of Technology, Boston, MA, USA) evaluations. The optimization process, which aimed at maximizing the DAWT power coefficient at low Reynolds numbers via diffuser cross-section optimization, is reported in a separate manuscript [40]. The present work focuses on generating wind tunnel measurements of lift, drag, and pressure distributions for the optimized airfoil at Reynolds numbers of 68k, 118k, and 159k, and on validating XFOIL predictions as well as RANS simulations (ANSYS, Inc., Canonsburg, PA, USA) using the fully turbulent k-ω SST model [57] and the γ-Re_θ transition model [58–60] against these experimental data.

The k-ω SST is a fully turbulent model. It assumes the boundary layer is turbulent from the leading edge onward. It cannot predict laminar flow or natural transition. However, γ-Re_θ (Transition SST) is a correlation-based transition model built on top of k-ω SST. It adds two transport equations: one for intermittency (γ) and one for transition momentum thickness Reynolds number (Re_θ). This allows it to predict where the flow transitions from laminar to turbulent.

2.1. Airfoil Geometry and Optimization Background

The custom airfoil was developed using a Response Surface Methodology (RSM) framework that integrated XFOIL [61] analyses within a CFD-driven design loop. The key geometric modifications from the baseline E423 included reducing the maximum thickness from 12.52% to 9.7%, increasing the maximum camber from 9.34% to 9.91%, decreasing the leading-edge radius by 39.2%, and reducing the trailing-edge angle by 22.5%. Detailed geometric parameters of the baseline and optimized airfoil are compared in Table 1, and an

overlay of both profiles is shown in Figure 2. The coordinates of the customized profile and original profile are published in our previous work [40].

Table 1. Comparison of Geometric Parameters between E423 and Custom E423 Airfoil.

Parameter	E423 Value	Custom Airfoil Value
Maximum Thickness	12.52% at 23.7% chord	9.7% at 24% chord
Maximum Camber	9.34% at 41.4% chord	9.91% at 44.8% chord
Camber Line Distribution	Symmetric increase to max, then decrease to trailing edge	Enhanced forward camber for better pressure recovery
Thickness Distribution	Peaks mid-chord, tapers to edges	Reduced overall for lower drag, with refined taper
Leading Edge Radius	0.0265	0.0161
Trailing edge angle	7.52°	5.83°

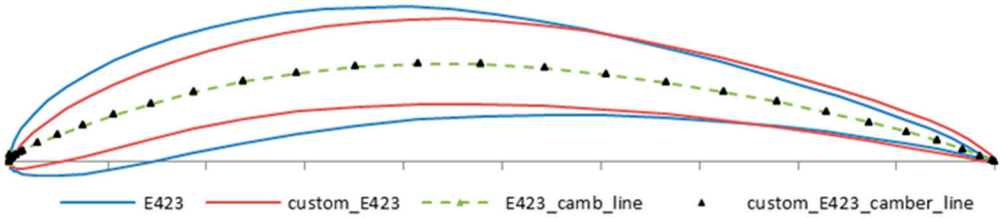

Figure 2. Overlay of original E423 (solid blue) and custom_E423 (red solid) airfoil profiles, with corresponding camber lines (dashed green and black triangles, respectively).

2.2. Experimental Facility

Experiments were conducted in the Adama Science and Technology University HM 170 open-circuit (Eiffel-type) low-speed wind tunnel [62]. As shown in Figure 3, the facility features a transparent test section with a square cross-section of 0.292 m × 0.292 m and a length of 0.42 m, and a model mount-in. The tunnel is equipped with a flow straightener and a contoured nozzle to ensure uniform flow. It is powered by a 2.2 kW axial fan with a variable speed drive, capable of generating freestream velocities from 2.8 m/s to 28 m/s.

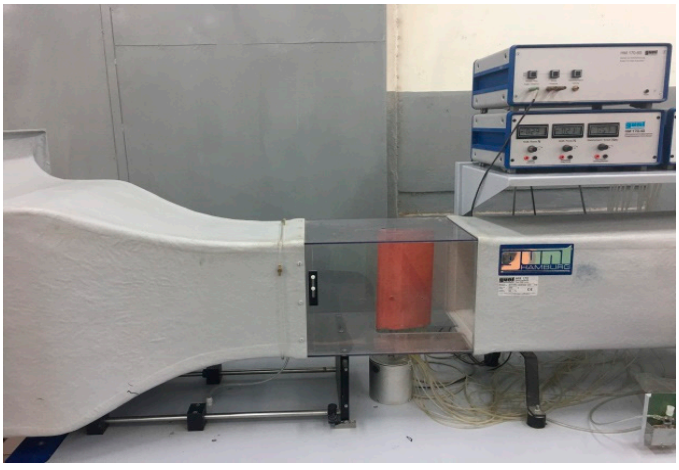

Figure 3. GUNT HM 170 wind tunnel and airfoil model mounted in the test section.

The Reynolds number is defined as $Re_c = \rho Vc/\mu$, where V is the freestream velocity (m/s), c = 0.15 m is the airfoil chord length, ρ = 0.9821 kg/m^3 is the air density at the test experiment site, and $\mu = 1.82 \times 10^{-5}$ Pa·s is the dynamic viscosity. The tested chord-based Reynolds numbers (Re_c = 68k, 118k, 159k) correspond to freestream velocities of approximately 8.4 m/s, 14.6 m/s, and 19.6 m/s, respectively. When related

to a 1 m diameter DAWT rotor, the target application for this customized airfoil, these same velocities yield rotor-based Reynolds numbers Re_D = ρVD/μ of approximately 4.5×10^5, 7.8×10^5, and 1.05×10^6, respectively, which are representative of small-scale DAWTs operating in low-wind-speed regions (annual average wind speeds of 3–7 m/s with gust peaks up to 20 m/s). Consequently, the tested Re_c range directly replicates the boundary layer transition behavior that the diffuser airfoil would experience under realistic rotor-scaled conditions.

2.3. Model Fabrication and Instrumentation

The optimized airfoil model, with a chord length of 0.15 m and span of 0.29 m, was fabricated using 3D printing with Polylactide (PLA) material [63–65], with a surface roughness of 0.08 mm. The 0.08 mm surface roughness (Ra ≈ 80 μm) is below the critical roughness for transition at these Reynolds numbers. For airfoils at Re ≈ 1×10^5, critical roughness typically exceeds 100 μm [28]. Thus, roughness-induced premature transition is unlikely. PLA is widely used for aerodynamic models due to its low cost, stiffness, dimensional accuracy, and eco-friendly properties [65].

The model was instrumented with 13 pressure taps (1.52 mm diameter) distributed along the chord at the mid-span location (Figure 4), following established practices for surface pressure measurement on 3D-printed airfoils [63,66]. The 13 pressure taps represent a practical compromise given the model chord and available instrumentation channels. However, the leading-edge region is under-resolved, where strong pressure gradients occur. This limitation is acknowledged, and the uncertainty in this region is higher (see Section 2.5). Lift and drag forces were measured using the integrated two-component electronic force sensor (±4 N). Surface pressures were acquired using the HM 170.60 data acquisition system [62].

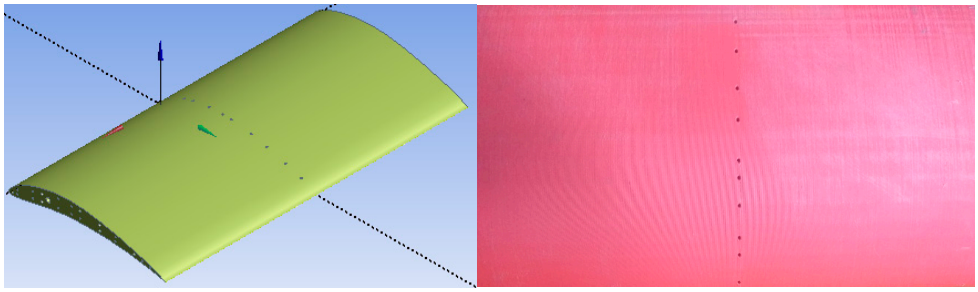

Figure 4. Isometric view (**left**) and 3D printed model (**right**) showing pressure taps at spanwise center (0.145 m).

2.4. Test Conditions and Procedure

Tests were performed at three Reynolds numbers: 68k, 118k, and 159k. The upper limit was selected for two reasons. First, the tested range (68k–159k) intentionally captures the low-Re transitional regime where LSB effects are most pronounced, and modeling is most challenging. Second, wind tunnel testing at velocities exceeding approximately 20 m/s induced structural vibrations, compromising measurement quality. Thus, Re = 159k represents the maximum safe and reliable operating condition for the present experimental apparatus. Notably, for a 1 m diameter DAWT rotor, this chord-based Re_c corresponds to a rotor-based Re_D = 1000k, which is representative of practical small-scale Wind-Lens systems in low-wind-speed regions. The angle of attack was varied from 0° to 17.5° in steps of 0°, 5°, 7.5°, 10°, 12.5°, 15°, and 17.5°. Calibration of the force sensor and velocity system was conducted before testing, and empty-tunnel runs were performed at each velocity to establish baseline conditions.

2.5. Uncertainty Analysis

Experimental uncertainties were considered in accordance with the AIAA Standard S-071A-1999 [67,68]. The primary sources of uncertainty considered are two-component force sensor accuracy (±0.5% of full scale over a ±4 N range), freestream velocity measurement [69] (±1.2%), and pressure transducer precision [70] (±0.1% of full scale).

The dimensionless force coefficients and the pressure coefficient are derived from the measured forces and pressure difference as shown in Equations (1)–(3).

$$CL = \frac{L}{\frac{1}{2}\rho V^2 A} \tag{1}$$

$$CD = \frac{D}{\frac{1}{2}\rho V^2 A} \tag{2}$$

$$Cp = \frac{\Delta P}{\frac{1}{2}\rho V^2} \tag{3}$$

where L and D are the measured lift and drag forces (N), ρ = 0.9821 kg/m^3 is the air density, V is the freestream velocity (m/s), A = c × span = 0.15 × 0.292 = 0.0435 m^2 is the planform area, and ΔP is the local surface pressure (Pa) measured at each pressure tap.

Accordingly, the maximum expanded uncertainties considered were ±2.1% for the lift coefficient CL, ±2.4% for the drag coefficient CD, and ±0.025 for Cp, following the experience of [68]. The uncertainty in Cp was largest near the leading edge due to high pressure gradients. All tests were repeated three times, and reported uncertainties are expanded uncertainties at a 95% confidence level, following the AIAA standard [67,71]. The maximum run-to-run variation in CL was ±1.2%, within the reported expanded uncertainty.

The geometric blockage ratio is 0.15 m/0.292 m = 0.51 (51%). Since the CFD domain replicated the experimental test section exactly, all confinement effects were inherently captured. Hence, no blockage corrections were applied, and the experimental uncertainty bands served as the validation reference for the numerical predictions.

2.6. Computational Setup

2.6.1. CFD in ANSYS Fluent

3D fully turbulent (k-wSST) and transitional (γ-Re_θ) RANS simulations were performed using ANSYS Fluent 2021 R1. The γ-Re_θ transition model used is ANSYS Fluent. The computational domain was designed to exactly replicate the experimental wind tunnel test section with a square cross-section of 0.292 m × 0.292 m. As shown in Figure 5, it was divided into four distinct regions to facilitate localized mesh control: Far Upstream Section (FUS) of 9.6c, near-wall region (NWR) of 1.67c containing the airfoil, Wake Region (WR) of 3.3c, and Far Downstream Section (FDS) of 15.3c. The total domain length is 30c, with flow directed from left to right (FUS to FDS). The 30c total length was selected to ensure the wake exits without recirculation at the outlet. A sensitivity study showed that increasing domain length beyond 25c changed CL by less than 0.1%.

The mesh was generated using ANSYS Fluent Meshing with a hybrid unstructured approach combining tetrahedral (the NWR) and hexahedral core elements and prismatic inflation layers, a method commonly applied in moderately complex geometries requiring boundary layer resolution [72] and successfully applied in CFD simulations [73]. As illustrated in Figure 6a–c, 15 inflation layers were applied on the airfoil surface with a first cell height of 1.9 × 10^{-5} m to maintain $y^+ \sim 1$ for the RANS model, with refined elements at the leading edge via edge sizing to resolve the stagnation point and suction peak. Inflation layers were also applied to the wind tunnel sidewalls (first cell height: 2.9 × 10^{-5} m) to resolve sidewall boundary layer effects, enabling direct correlation with experimental

data. Gradual mesh coarsening toward far-field boundaries is shown in the isometric view (Figure 6a), while the sectional view (Figure 6b) illustrates the mid-span plane topology.

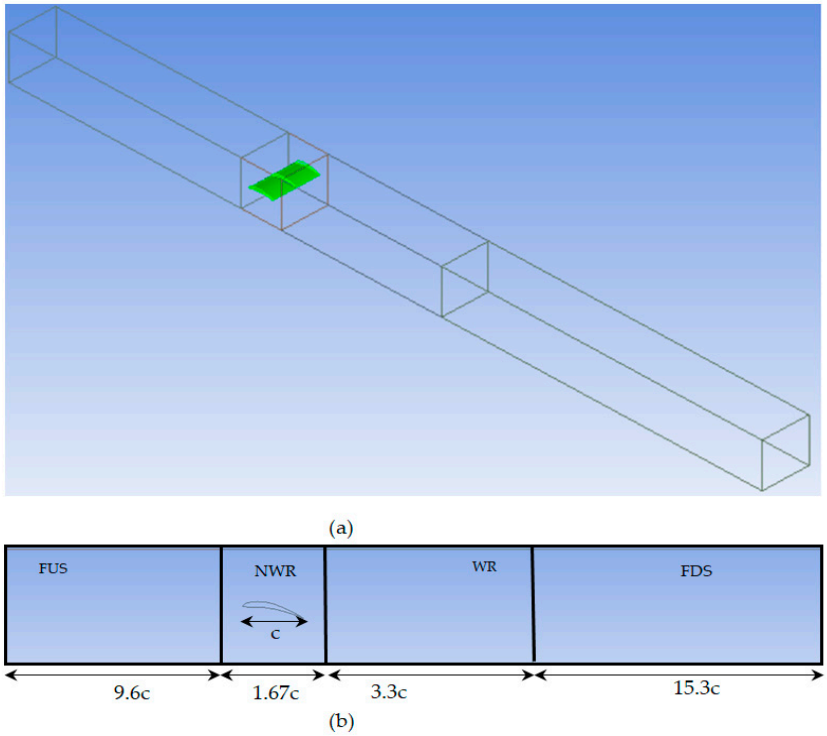

Figure 5. Computational domain of CFD simulation. (**a**) Isometric view showing the airfoil (green) inside the wind tunnel. (**b**) Mid-plane section view to show dimensions.

A mesh independence study was conducted using three grid resolutions, including coarse (2.85 million cells), medium (5.2 million cells), and fine (7.5 million cells), following established grid convergence methodologies [74]. As shown in Figure 7, increasing mesh density beyond 5.0 million cells resulted in less than 0.15% variation in CL and less than 0.50% variation in CD. The medium mesh (5.2 million cells) was selected as it provides grid-independent results, balancing accuracy and computational cost. In addition, the mesh quality metrics were checked to ensure numerical stability and solution accuracy [74], achieving minimum orthogonal quality greater than 0.1, maximum skewness just over 0.9, maximum aspect ratio below 95, and minimum element quality above 0.02.

Both the fully turbulent k-ω SST turbulence model [57] and the γ-Re_θ transition model [58–60] were employed to accurately capture laminar-to-turbulent transition effects at low Reynolds numbers, following the modeling framework previously validated in our earlier work [40]. Accordingly, a pressure-based solver was used for incompressible flow with air properties matching the experiments (ρ = 0.9821 kg/m^3, $\mu = 1.82 \times 10^{-5}$ Pa·s). Boundary conditions included a velocity inlet with uniform velocity corresponding to the experimental conditions (turbulence intensity = 0.1%, turbulent viscosity ratio = 1), a pressure outlet with zero gauge pressure, and no-slip conditions on the airfoil and tunnel walls. The freestream turbulence intensity was set to 0.1% in CFD; a sensitivity test with 0.5% changed CL by less than 1%, confirming that the exact value is not critical for comparative validation. Solution methods employed coupled pressure–velocity coupling, second-order upwind discretization for pressure and momentum equations, and first-order upwind for turbulence quantities, the same numerical scheme as adopted in [40]. First-order upwind discretization was used for turbulence transport equations to ensure numerical stability, as per the recommendations of [40]. A test case at Re = 118k, $\alpha = 10°$, using second-order upwind for turbulence quantities changed CL by less than 1%, confirming

negligible numerical diffusion effects for the present conclusions, a finding that mirrors the verification performed in [40]. Convergence was monitored through residuals below 10^{-4} and stabilization of CL and CD values, with the convergence criterion set to 1×10^{-4} for all residuals, directly following [40]. A tighter criterion of 1×10^{-6} for energy and 1×10^{-5} for turbulence quantities was tested for a subset of conditions (Re = 118k, $\alpha = 10°$) and changed Cp by less than 0.004; therefore, the 1×10^{-4} criterion is sufficient for force coefficient predictions, fully consistent with the convergence strategy established in [40].

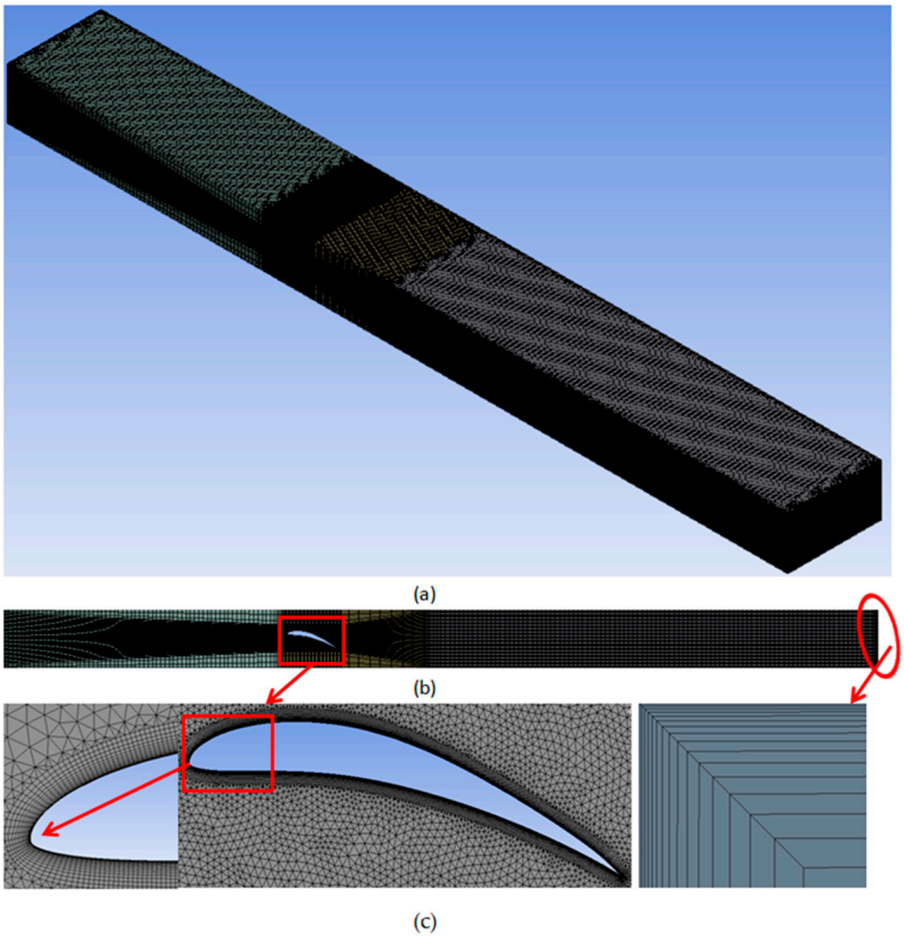

Figure 6. Mesh topology for the computational domain. (**a**) Isometric view; (**b**) mid-span sectional view; (**c**) detailed near-airfoil view (**left**); side view, showing inflation around the tunnel wall (**right**).

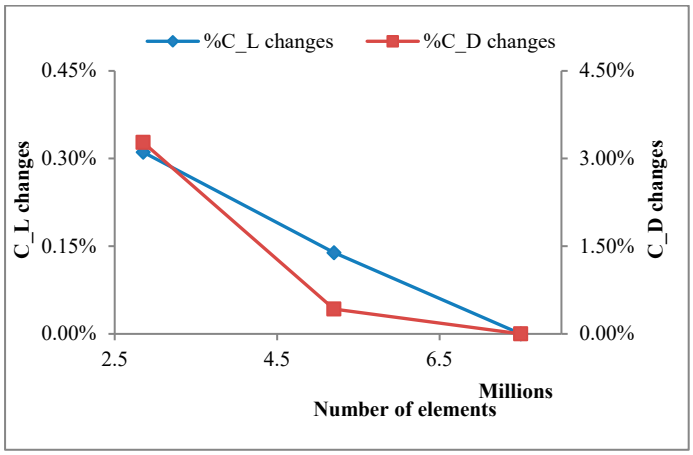

Figure 7. Grid Independence Study as a Function of Mesh Elements (in Millions) Combined CL and CD.

2.6.2. XFoil

XFOIL is a coupled viscous-inviscid panel method widely used for low-Reynolds-number airfoil analysis due to its computational efficiency and reasonable accuracy for attached and mildly separated flows. The inviscid flow is solved using a linear-vorticity stream function panel method with a Karman–Tsien compressibility correction, while the viscous boundary layer and wake are modeled using an integral boundary layer formulation based on a two-equation lagged dissipation integral method. Transition is predicted using the envelope e^n method, where the user-specified critical amplification factor Ncrit determines the sensitivity to freestream disturbances. The viscous and inviscid solutions are coupled through a transpiration model that accounts for the displacement effect of the boundary layer on the outer potential flow, solved simultaneously using a global Newton method. XFOIL version 6.99 [61] was used with 200 panels in viscous mode and Ncrit = 9 for free transition. The Ncrit = 9 value corresponds to standard wind tunnel turbulence levels. Simulations were performed at the same Reynolds numbers and angles of attack as the other CFD models and wind tunnel experiments.

2.7. Governing Equations and Model Differences

2.7.1. Reynolds-Averaged Navier–Stokes (RANS) Equations

Both k-ω SST and γ-Re_θ models solve the Reynolds-averaged Navier–Stokes equations, which govern the mean flow quantities by decomposing the instantaneous flow variables into time-averaged and fluctuating components. For incompressible, steady flow without body forces, the continuity and momentum (RANS) equations are expressed as:

Continuity equation:

$$\frac{\partial \overline{u}_i}{\partial t} = 0 \tag{4}$$

Momentum equation:

$$\rho\left[\frac{\partial \overline{u}_i}{\partial t} + \overline{u}_j \frac{\partial \overline{u}_i}{x_j}\right] = -\frac{\partial \bar{p}}{\partial x_i} + \frac{\partial}{\partial x_j}\left(\mu \frac{\partial \overline{u}_i}{\partial x_j} - \rho\,\overline{u_i' u_j'}\right) + \rho f_i \tag{5}$$

where $\overline{u}_i$ and $\overline{u}_j$ are the time-averaged velocity components, $\bar{p}$ is the mean pressure, μ is the dynamic viscosity, and $\overline{u_i' u_j'}$ represents the Reynolds stress tensor arising from the turbulence fluctuations. The Reynolds stresses introduce a closure problem, requiring additional transport equations to model the turbulent viscosity. The key difference between the two RANS models lies in how they treat the laminar-to-turbulent transition. The standard k-ω SST model assumes fully turbulent flow throughout the boundary layer, while the γ-Re_θ transition model incorporates two additional transport equations (intermittency γ and transition momentum thickness Reynolds number Re-θ_t) to predict the onset and extent of transition, making it more suitable for low-Reynolds-number flows where laminar separation bubbles (LSBs) are present.

The transport equations for the turbulent kinetic energy k and the specific dissipation rate ω in the k-ω SST model are given by Equations (6) and (7), respectively.

$$\rho\frac{\partial k}{\partial t} + \rho u_i \frac{\partial k}{\partial x_i} = \frac{\partial}{\partial x_j}\left(\Gamma_K * \frac{\partial k}{\partial x_j}\right) + \bar{G}^k - \gamma_k + S \tag{6}$$

$$\rho\frac{\partial \omega}{\partial t} + \rho u_i \frac{\partial \omega}{\partial x_i} = \frac{\partial}{\partial x_j}\left(\Gamma_\omega * \frac{\partial \omega}{\partial x_j}\right) + G_\omega - \gamma_\omega + D_\omega + S \tag{7}$$

where Γ_K and Γ_ω represent the effective diffusivity of k and ω, respectively; G_ω denotes the generation of ω due to turbulence production; γ_ω and γ_k represent the dissipation of

ω and k caused by turbulence; S is the source term; and Dω is the cross-diffusion term that arises when blending the k-ω and k-ε models. $\bar{G}^k$ corresponds to the production of turbulent kinetic energy.

The γ-Re_θ transition model supplements the k-ω SST turbulence model with two additional transport equations: one for the intermittency (γ) and one for the transition momentum thickness Reynolds number ($Re_{\theta t}$). These equations enable the model to predict the onset and length of the laminar-to-turbulent transition region. The equations used to calculate Intermittency transport and Transition momentum thickness Reynolds number transport are presented in Equations (8) and (9).

$$\frac{\partial(\rho\gamma)}{\partial t} + \frac{\partial(\partial\rho u_j\gamma)}{\partial x_j} = P_\gamma - E_\gamma + \frac{\partial}{\partial x_j}\left[\left(\mu + \frac{\mu_t}{\sigma_f}\right)\left(\frac{\partial\gamma}{\partial x_j}\right)\right] \quad (8)$$

$$\frac{\partial}{\partial t}(\rho\widetilde{Re_{\theta t}}) + \frac{\partial}{\partial x_j}(\rho u_j\widetilde{Re_{\theta t}}) = P_{\theta t} + \frac{\partial}{\partial x_j}\left[\sigma_{\theta t}(\mu + \mu_t)\left(\frac{\partial\widetilde{Re_{\theta t}}}{\partial x_j}\right)\right] \quad (9)$$

where P_γ and E_γ are the production and destruction terms of intermittency, respectively. The intermittency γ represents the fraction of time that the flow is turbulent at a given point, ranging from γ = 0 (fully laminar) to γ = 1 (fully turbulent); $P_{\theta t}$ is the production source term designed to drive the transported scalar $\widetilde{Re_{\theta t}}$ toward the local value of the transition momentum thickness Reynolds number $Re_{\theta t}$ computed from an empirical correlation, $\sigma_{\theta t}$ model constant, in the transport equation for the transition momentum thickness Reynolds. Transition is predicted to occur when the boundary layer vorticity Reynolds number is the local $\widetilde{e_{\theta t}}$.

2.7.2. Model Comparison

The three models differ fundamentally in their mathematical formulation, domain treatment, transition prediction, separation handling, and computational cost. Understanding these differences is essential for interpreting the validation results presented later, as each model's strengths and limitations directly influence its predictive accuracy. Table 2 summarizes these key methodological differences.

Table 2. Methodological differences among the three modeling approaches evaluated in this study.

Feature	XFOIL	k ω SST (Fully Turbulent)	γ Re_θ (Transition)
Governing equations	Potential flow + integral boundary layer	Full RANS equations	Full RANS equations
Domain	Inviscid outer + thin boundary layer	Entire flow field	Entire flow field
Transition prediction	e^n method (user-defined Ncrit)	None (assumes fully turbulent)	γ Re_θ transport equations
Separation handling	Limited (small bubbles only)	Full separation captured	Full separation captured
Computational cost	Very low (seconds)	Moderate to high (hours)	Moderate to high (hours)
Best suited for	Attached/mildly separated flows	Fully turbulent attached/separated flows	Transitional flows with LSB

2.8. Validation Approach

The experimental data served as the reference for validating both XFOIL and RANS predictions. Quantifying the agreement between CFD simulations and experimental measurements requires a comprehensive set of error metrics to capture distinct aspects of model performance. The mean absolute error (MAE) and root mean square error (RMSE) provide absolute measures of deviation in the original units, with RMSE being particularly

sensitive to larger discrepancies. The mean absolute percentage error (MAPE) offers a scale-independent relative assessment, while the percent error (PE) is well-suited for point-wise comparisons. Bias reveals systematic over- or underprediction tendencies, whereas the coefficient of determination (R^2) and Pearson's correlation coefficient (r) quantify the proportion of variance explained and the strength of the linear relationship between predicted and measured values.

This multi-metric approach ensures a robust validation of the numerical models against experimental observations. The quantitative evaluation followed best practices established in the literature [27,44,45], and the mathematical formulations of the validation metrics are presented in Table 3.

Table 3. Quantitative validation metrics used to assess CFD model performance against experimental data, with corresponding formulas, units, optimal applications, and inherent weaknesses.

Metrics and Formula	Units	Measures	Weakness
$PE = \left\lvert \frac{\varnothing_{num,i} - \varnothing_{exp,i}}{\varnothing_{exp,i}} \right\rvert \times 100$	%	Relative error magnitude	Fails near zero
$MAPE = \frac{1}{n} \sum_{i=n}^{n} \left\lvert \frac{\varnothing_{num,i} - \varnothing_{exp,i}}{\varnothing_{exp,i}} \right\rvert \times 100$	%	Average relative error	Undefined at zero
$MAE = \frac{1}{n} \sum_{i=1}^{n} \lvert \varnothing_{num,i} - \varnothing_{exp,i} \rvert$	Same as variables	Average error magnitude	Ignores error distribution
$RMSE = \sqrt{\frac{1}{n} \sum_{i=1}^{n} \left(\varnothing_{num,i} - \varnothing_{exp,i} \right)^2}$	Same as variables	Penalizing large errors	Sensitive to outliers
$Bias = \frac{1}{n} \sum_{i=1}^{n} \left(\varnothing_{num,i} - \varnothing_{exp,i} \right)$	Same as variables	Systematic error	Canceling errors gives zero
$R^2 = 1 - \frac{\sum_{i=1}^{n} \left(\varnothing_{num,i} - \varnothing_{exp,i} \right)^2}{\sum_{i=1}^{n} \left(\varnothing_{exp,i} - \overline{\varnothing}_{exp} \right)^2}$	-	Trend capture	High r accuracy
$r = \frac{\left[\sum_{i=}^{n} \left(\varnothing_{exp,i} - \overline{\varnothing}_{\_exp} \right) \left(\varnothing_{num,i} - \overline{\varnothing}_{\_num} \right) \right]}{\left[\sum_{i=1}^{n} \left(\varnothing_{exp,i} - \overline{\varnothing}_{\_exp} \right)^2 \right]^{\frac{1}{2}} \left[\sum_{i=1}^{n} \left(\varnothing_{num,i} - \overline{\varnothing}_{\_num} \right)^2 \right]^{\frac{1}{2}}}$		Strength & direction of linear correlation	Linear relationship strength

3. Results

This section presents the aerodynamic performance characterization of the custom airfoil by experimental method and the validation of three predictive models. Before analyzing the details, the near-wall grid resolution is presented to indicate the reliability of the numerical approach. The three models are compared against the experimental benchmark dataset, across Re = 68k, 118k, and 159k, and angles of attack 5°, 10°, 12.5°, and 17.5°. Force coefficient analysis is conducted qualitatively through comparison of polar curves and quantitatively using error metrics to evaluate model reliability. Similarly, pressure coefficient distributions are presented across the chord-wise location on both the upper and lower surfaces to provide insight into boundary layer behavior, separation characteristics, and the accuracy of each predictive model in capturing surface pressure. Finally, sensitivity analyses further examine the influence of Reynolds number and angle of attack on aerodynamic coefficients.

3.1. Numerical Convergence and Near-Wall Mesh Resolution

Before analyzing the flow, the numerical convergence and near-wall mesh resolution were verified at Re = 118k. Figure 8 presents the residual convergence history for the γ-Re_θ and k-ω SST models. The γ-Re_θ model achieves a steady reduction in residuals,

which indicates a converged steady-state solution (Figure 8a). The k-ω SST model exhibits persistent oscillations, with residuals plateauing (Figure 8b). This behavior is typical for fully turbulent simulations of airfoils at low Reynolds numbers.

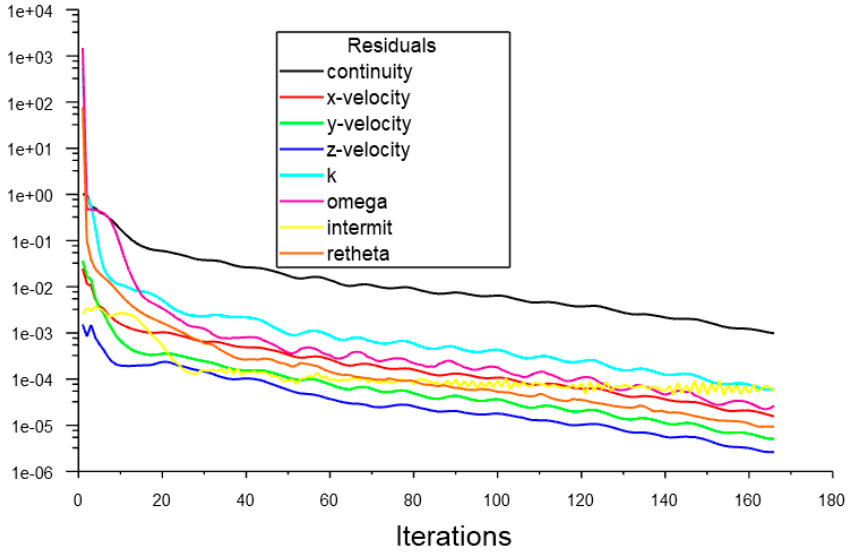

(**a**) γ-Re_θ

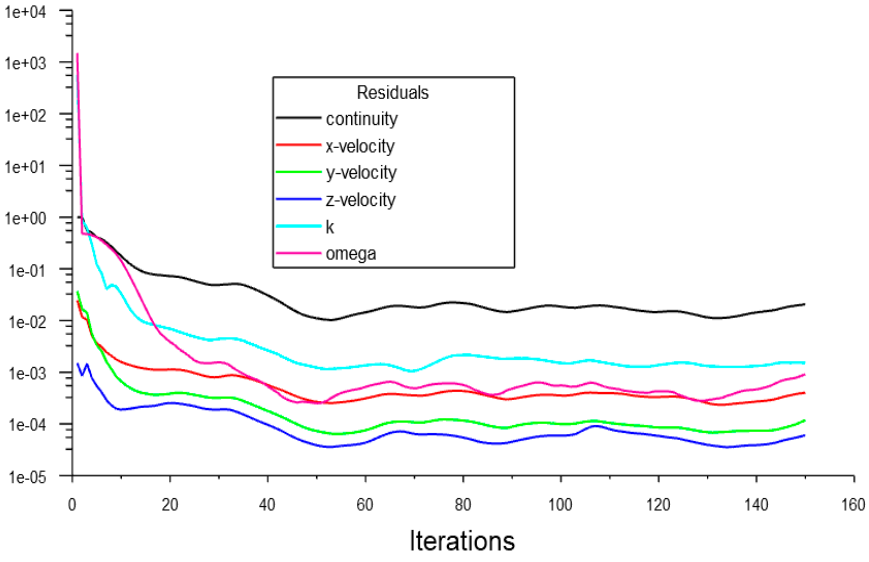

(**b**) k−-ω SST

Figure 8. Convergence history of residuals for (**a**) the γ-Re_θ (Transition SST) model and (**b**) the k-ω SST model.

Following convergence verification, the near-wall mesh resolution was evaluated. Figure 9 shows the y^+ distribution on the airfoil surface for both turbulence models at the same operating conditions. For the γ-Re_θ model (a), the y^+ at the leading-edge stagnation point reaches a maximum of 0.85 immediately downstream of stagnation. For the k-ω SST model (b), the maximum value is 0.96. Both models satisfy near-wall resolution requirements. The maximum y^+ values are 0.85 (γ-Re_θ) and 0.96 (k-ω SST), both well within the recommended limit of 1.0. The highest y^+ occurs on the suction side near the leading edge due to flow acceleration.

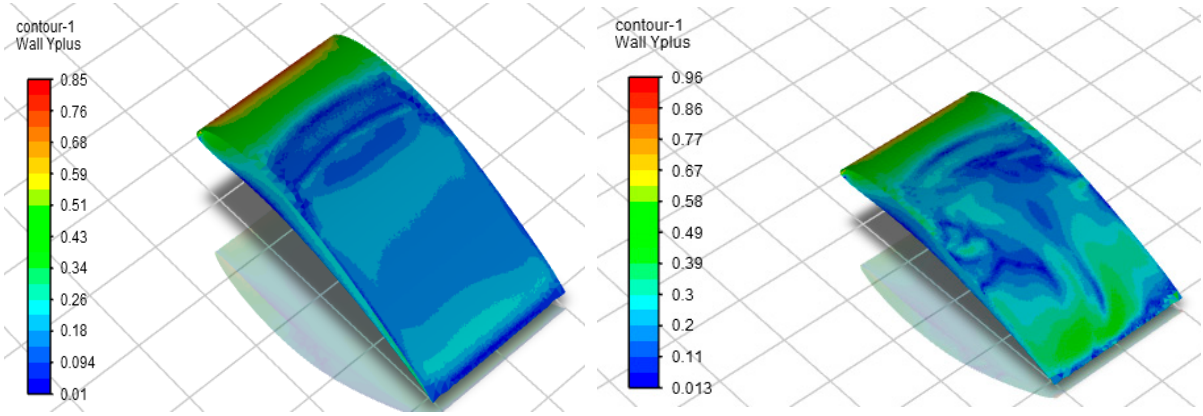

(**a**) γ-Re_θ (**b**) k-ω SST

Figure 9. Contours of wall y^+ distribution on the airfoil surface (**a**) = γ-Re_θ, (**b**) = k-ω SST.

3.2. Force Coefficients

3.2.1. Key Aerodynamic Performance Parameters

The maximum lift coefficient, stall angle, maximum lift-to-drag ratio, and the angle at which this maximum occurs are extracted from the experimental and computational data to compare the key aerodynamic characteristics of each model. Table 4 summarizes these parameters across the tests. The complete raw CL and CD values used to analyze the force coefficinets are available in Supplementary Dataset Table S1.

Table 4. Summary of Key Aerodynamic Performance Parameters.

Re	Method	CL_Max	α_Stall (°)	(CL/CD)_Max	% Error CL_Max.
68k	Experiment	1.5389	15	16.93	—
	XFOIL	1.4419	17.5 *	10.12	−6.3
	k-ω SST	1.6895	17.5 *	48.79	+9.8
	γ-Re_θ	1.5324	15	17.83	−0.4
118k	Experiment	1.7523	15	32.42	—
	XFOIL	1.6649	15	57.48	−5.0
	k-ω SST	1.7963	15	49.74	+2.5
	γ-Re_θ	1.7480	15	44.43	−0.2
159k	Experiment	1.7630	15	36.36	—
	XFOIL	1.8477	12.5	58.72	+4.8
	k-ω SST	1.7907	15	39.07	+1.6
	γ-Re_θ	1.7718	12.5	42.34	+0.5

*Note: * means stall not reached within test range, and k denotes thousands.*

The experimental maximum lift coefficients fall within the range reported for high-camber low-Re airfoils. Similar results were reported by Selig and Guglielmo [34], who reported CL = 1.65–1.85 for the S1223 airfoil at Re = 100k–200k. The present custom profile achieves CL_max = 1.54–1.763 across Re = 68k–159k. It demonstrated consistent high-lift performance across the tested range.

The stall angle is typical for high-camber low-Re airfoils [35]. The Reynolds number insensitivity of stall angle observed here is consistent with findings from Rogowski et al. [16] for the NACA 0018 airfoil, where stall angle becomes Reynolds number independent above Re ≈ 60k.

XFOIL underpredicted CL_max at Re = 68k and overpredicted at Re = 159k. Stall angle prediction is accurate at Re = 118k but predicts an earlier stall at Re = 159k. The k-ω SST model overpredicts CL_max by 9.8% at Re = 68k but improves to within 2.5% at higher Reynolds numbers. The γ-Re_θ transition model exhibits the closest agreement

with experimental CL_max values across all test conditions, with errors consistently below 0.5%. Stall angle prediction is accurate except at Re = 159k, where it predicts an earlier stall angle. The maximum lift-to-drag ratio is consistently achieved at 5° angle of attack for all models except XFOIL at Re = 118k and k-ω SST at Re = 159k.

3.2.2. Percentage Error of CL and CD

The accuracy of the CFD predictions is quantified by calculating the percentage error relative to the experimental measurements at each angle of attack. Figures 10–12 present the lift and drag coefficients as functions of the angle of attack for Re = 68k, 118k, and 159k, respectively, comparing experimental data (exp) against the three models. Table 5 reports the MAPE for each model at these Reynolds numbers; the corresponding percentage errors at each angle of attack are given in Appendix A.

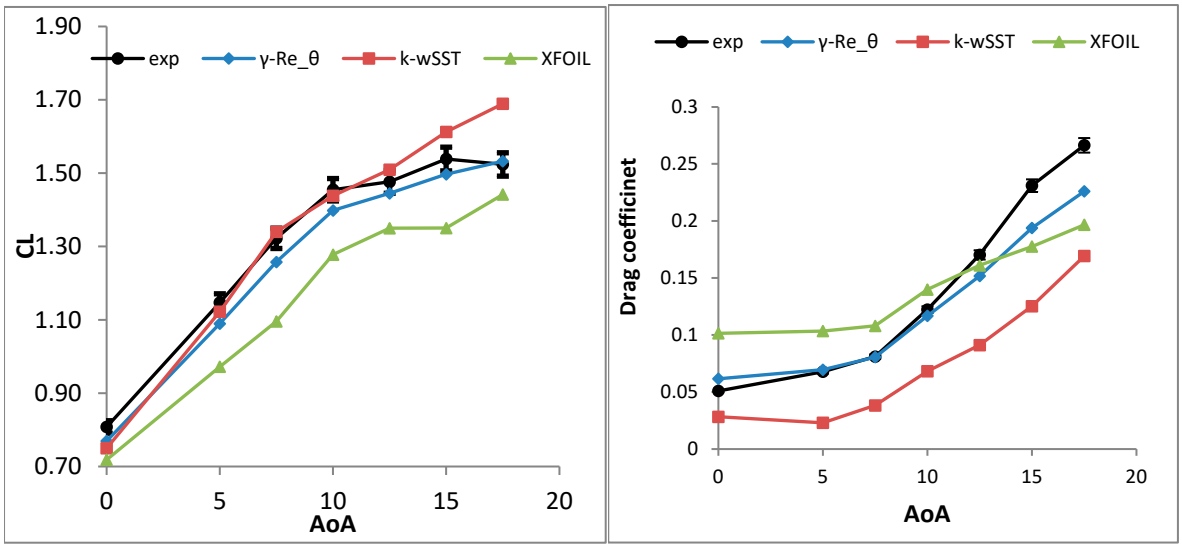

Figure 10. Lift (**left**) and drag (**right**) coefficient predictions at Re = 68k, comparing experimental data against XFOIL, k-ω SST, and γ-Re_θ models.

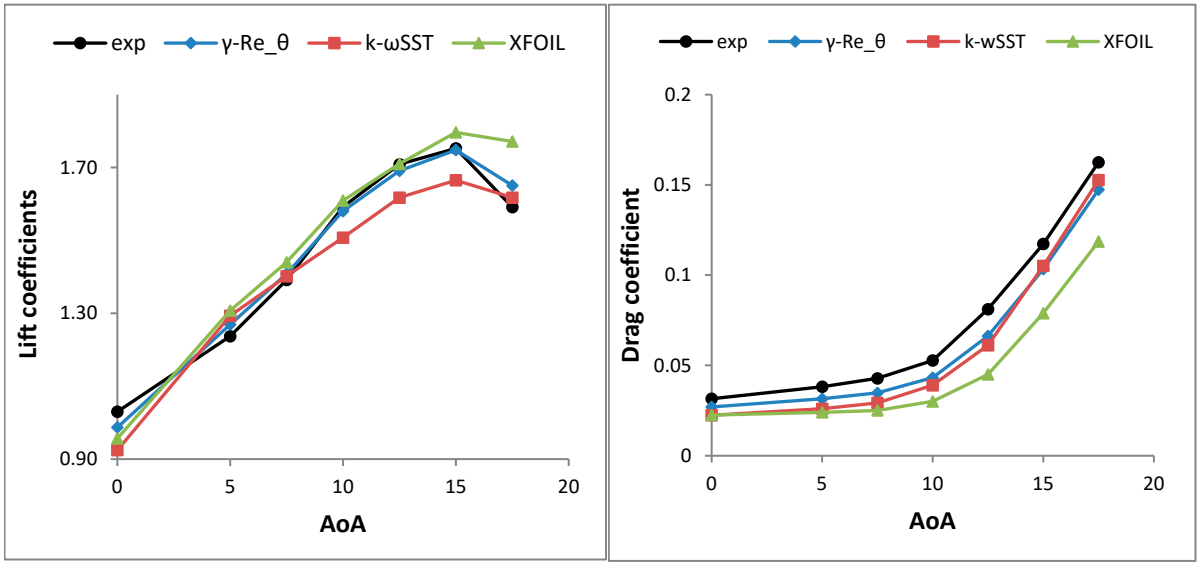

Figure 11. Lift (**left**) and drag (**right**) coefficient predictions at Re = 118k, comparing experimental data against XFOIL, k-ω SST, and γ-Re_θ models.

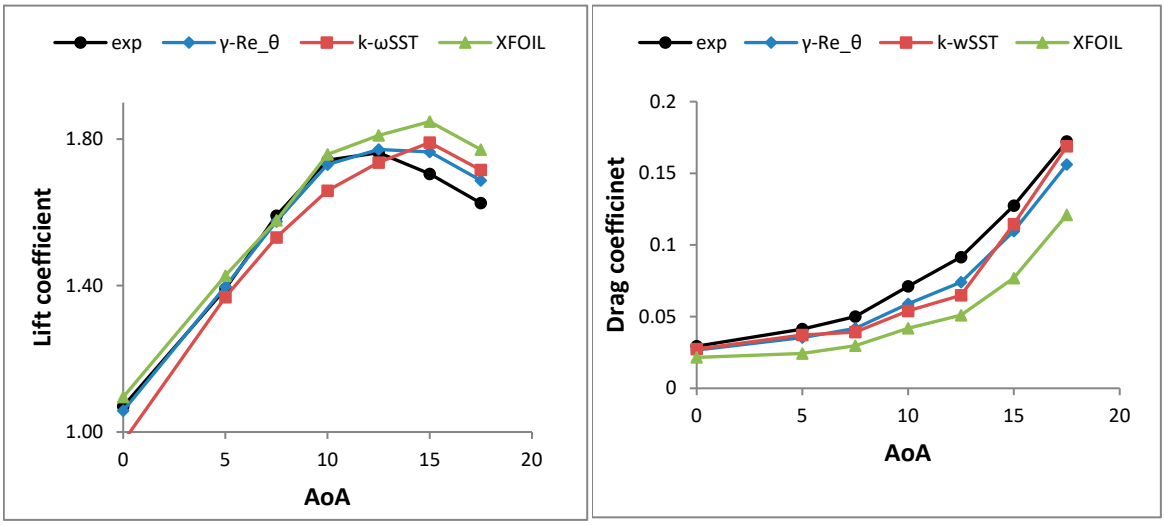

Figure 12. Lift (**left**) and drag (**right**) coefficient predictions at Re = 159k, comparing experimental data against XFOIL, k-ω SST, and γ-Re_θ models.

Table 5. Mean absolute percentage error (MAPE) for each model at Re = 68k, 118k, and 159k. Visual trends corresponding to these errors are shown in Figures 10–12. Detailed percentage errors at each angle of attack are provided in Appendix A.

Re	XFOIL		k-ω SST		γ-Re_θ	
	CL	CD	CL	CD	CL	CD
68k	11.51	36.31	4.25	48.04	3.42	10.12
118k	4.47	36.34	4.69	22.83	1.96	15.45
159k	3.82	37.61	4.46	14.82	1.57	14.23

In Figure 10, the lift (left) and drag (right) coefficient predictions at Re = 68k are comparatively presented. For lift, the γ-Re_θ transition model closely follows the experimental curve, while XFOIL substantially underpredicted for AoA. For drag, the k-ω SST model also underpredicts angles of attack. Quantitatively, Table 5 confirms these observations: γ-Re_θ achieves the lowest lift MAPE (3.42%), compared to XFOIL's 11.51% and k-ω SST's 4.25%; for drag, γ-Re_θ maintains a MAPE of 10.12%, whereas k-ω SST shows a very high error of 48.04% and XFOIL 36.31%.

Figure 11 presents the lift (left) and drag (right) predictions at Re = 118k. For lift, all models perform reasonably well, though γ-Re_θ appears slightly closer to the experimental data across most angles. For drag, the model consistently underpredicts and shows a uniform trend, while XFOIL's prediction is the worst. According to Table 5, γ-Re_θ achieves the lowest lift MAPE (1.96%), compared to 4.69% for k-ω SST and 4.47% for XFOIL; for drag, γ-Re_θ attains a MAPE of 15.45%, which is better than k-ω SST (22.83%) and XFOIL (36.34%).

In Figure 12, the trend observed for both coefficients closely agrees with the observation at the Re = 159k case. For lift, all three models show improved agreement compared to lower Reynolds numbers, but γ-Re_θ remains the most accurate, with a slight deviation around and aft stall. For drag, both RANS models' prediction was close to each other. However, the k-ω SST model improves significantly at this higher Reynolds number. As seen in Table 5, γ-Re_θ achieves a lift MAPE of only 1.57%, k-ω SST 4.46%, and 3.82% for XFOIL; for drag, k-ω SST attains a MAPE of 14.82%, close to γ-Re_θ's 14.23%, while XFOIL remains poor at 37.61%.

3.2.3. Statistical Metrics and Sensitivity Analysis of Prediction Accuracy

Comprehensive statistical metrics provide a detailed assessment of model performance, capturing correlation, error magnitude, and systematic bias. Table 6 summarizes these metrics for each model across the Reynolds numbers. Together with a sensitivity analysis of Reynolds number and angle of attack, these metrics serve to evaluate prediction accuracy under varying flow conditions.

Table 6. Quantitative Validation Metrics across Re.

Re	Metrics	XFOIL		k-ω SST		γ-Re_θ	
		CL	CD	CL	CD	CL	CD
68k	R^2	0.968	0.814	0.992	0.954	0.996	0.992
	MAE	0.1320	0.0426	0.0485	0.0531	0.0389	0.0187
	RMSE	0.1569	0.0518	0.0605	0.0584	0.0456	0.0213
	Bias	−0.1127	−0.0133	+0.0107	−0.0467	−0.0265	−0.0089
118k	R^2	0.994	0.935	0.998	0.974	0.999	0.994
	MAE	0.0579	0.0201	0.0579	0.0146	0.0287	0.0069
	RMSE	0.0808	0.0218	0.0705	0.0189	0.0356	0.0084
	Bias	+0.0119	−0.0151	−0.0198	−0.0116	−0.0031	−0.0052
159k	R^2	0.988	0.916	0.998	0.984	0.999	0.996
	MAE	0.0789	0.0193	0.0595	0.0074	0.0234	0.0058
	RMSE	0.1074	0.0218	0.0701	0.0103	0.0289	0.0072
	Bias	−0.0079	−0.0151	−0.0178	−0.0018	+0.0052	−0.0041

Lift Coefficient Predictions

In Table 6, the models' correlation with experiment and error characteristics in predicting the CL is presented. All three models exhibit excellent correlation with experimental data in predicting the lift coefficient across Re. Both RANS models achieve $R^2 > 0.99$ across all conditions. XFOIL achieves $R^2 > 0.99$ at Re = 118k; however, it drops to $R^2 = 0.968$ at Re = 68k, indicating difficulty in transitional flow regimes.

The γ-Re_θ transition model achieves the lowest MAE across Re; the RMSE values marginally exceed the MAE, which indicates well-distributed errors. Bias remains near-zero across all conditions, except at Re = 68k (−0.0265). The k-ω SST model exhibits higher MAE values (0.0485–0.0595) and a wider MAE-RMSE gap compared to the transition model and better than XFOIL. The prediction bias shifts from positive at Re = 68k (+0.0107) to negative at higher Re (−0.0198 to −0.0178). This shows a systematic offset that varies with the flow regime. XFOIL matches the k-ω SST model accuracy at Re = 118k (MAE = 0.0579) but deteriorates sharply at Re = 68k, and the MAE-RMSE gap widens considerably.

Drag Coefficient Predictions

The discrepancy in the models' ability and error characteristics in capturing drag physics is presented in Table 6. The γ-Re_θ transition model maintains excellent agreement with experimental data across all Reynolds numbers, followed by the full turbulent model, except at Re = 68k ($R^2 = 0.954$). XFOIL exhibits consistently poor correlation across all conditions, with R^2 values between 0.814 and 0.935. It fails to represent the physical mechanisms governing drag generation in transitional flow.

Analyzing error, the γ-Re_θ transition model demonstrates better accuracy, with MAE remaining below 0.02 across conditions, and a small RMSE-MAE gap confirms uniformly distributed errors without severe local discrepancies across Re. However, the k-ω SST model exhibits pronounced MAE variation with Reynolds number, and the large negative bias at Re = 68k (−0.0467) indicates systematic underprediction of drag in transitional flow. This result is consistent with the fully turbulent assumption eliminating the LSB, which

in reality generates additional pressure drag. The model therefore produces lower drag than experimentally measured, not excessive drag. XFOIL displays the worst MAE values among the three models, though its MAE at Re = 68k (0.0426) is lower than that of the k-ω SST model.

Reynolds Number Sensitivity

The sensitivity of each model's predictive accuracy to Reynolds number is defined as the difference in MAE between the lowest and highest test Reynolds numbers (MAE at 68k minus MAE at 159k). Negative values indicate improving performance with increasing Reynolds number. Table 7 summarizes the Re sensitivity of error.

Table 7. Reynolds Number Sensitivity (MAE_{68_k}–MAE_{159_k}).

Model	CL Sensitivity	CD Sensitivity
XFOIL	+0.0531	+0.0233
k-ω SST	−0.0110	+0.0457
γ-Re_θ	+0.0155	+0.0129

As seen in Table 7, XFOIL exhibits high sensitivity in lift (increase of 0.0531) and drag coefficients (increase of 0.0233), showing both errors increase with Re. The k-ω SST model shows highly deteriorated drag predictions, while CL accuracy slightly improves with Re. The γ-Re_θ transition model demonstrates the most balanced sensitivity to Reynolds number variations, showing reduced accuracy as Re increases.

Angle of Attack Sensitivity

Angle sensitivity, defined as the change in MAE from 0° to 17.5°, quantifies how model accuracy varies with AoA. Values represent the difference in MAE between 17.5° and 0°. Negative values indicate improving accuracy with increasing angle, while positive values indicate degrading accuracy. Table 8 presents these sensitivity metrics across all Reynolds numbers.

Table 8. Angle of Attack Sensitivity ($MAE_{17.5}$–MAE_{0}°).

Model	Coeff.	Re = 159k	Re = 118k	Re = 68k	Mean
XFOIL	CL	+0.0432	+0.0652	+0.0668	+0.0584
	CD	−0.0009	−0.0278	−0.0514	−0.0267
k-ω SST	CL	−0.0600	−0.1037	−0.0145	−0.0594
	CD	−0.0029	−0.0131	−0.0141	−0.0100
γ-Re_θ	CL	+0.0146	−0.0052	−0.0241	−0.0049
	CD	−0.0021	−0.0148	−0.0250	−0.0140

XFOIL and k-ω SST exhibit the large mean lift sensitivity, +0.0584 and −0.0594, respectively, with opposite directions. The k-ω SST improved with increasing Re, while XFOIL degraded. Similarly, drag sensitivity is indicated by improved prediction with AoA for both models. The γ-Re_θ transition model demonstrates the most stable performance across the incidence range, with near-zero mean lift sensitivity (−0.0049) and drag sensitivity (−0.0140). This indicates minimal variation in accuracy from attached flow to post-stall conditions.

3.3. Pressure Coefficient Validation

A comprehensive assessment of predictive models' capabilities is presented through qualitative figures, quantitative tables such as overall validation metrics, angle-resolved

errors, chord-wise error distributions, Reynolds number sensitivity analysis, and percent error assessment across the test conditions. The complete raw supporting values used to this section are available in Supplementary Dataset Table S1.

3.3.1. Validation Summary of Cp

Table 9 presents the overall validation metrics for Cp predictions across all angles of attack at each Reynolds number, including bias, mean absolute error, root mean square error, maximum local error, and coefficient of determination (R^2). These metrics provide a comprehensive assessment of each model's ability to replicate experimental pressure distributions on both the upper and lower surfaces.

To complement the quantitative metrics in Table 9, Figure 13 presents the chord-wise Cp distributions for the most challenging transitional case (Re = 68k) at four angles of attack: 5°, 10°, 12.5°, and 17.5°. Within each panel, the upper and lower surface Cp are plotted against normalized chord position x/c, comparing experimental data against prediction models. The corresponding distributions at Re = 118k and Re = 159k are provided in Appendix B (Figures A1 and A2).

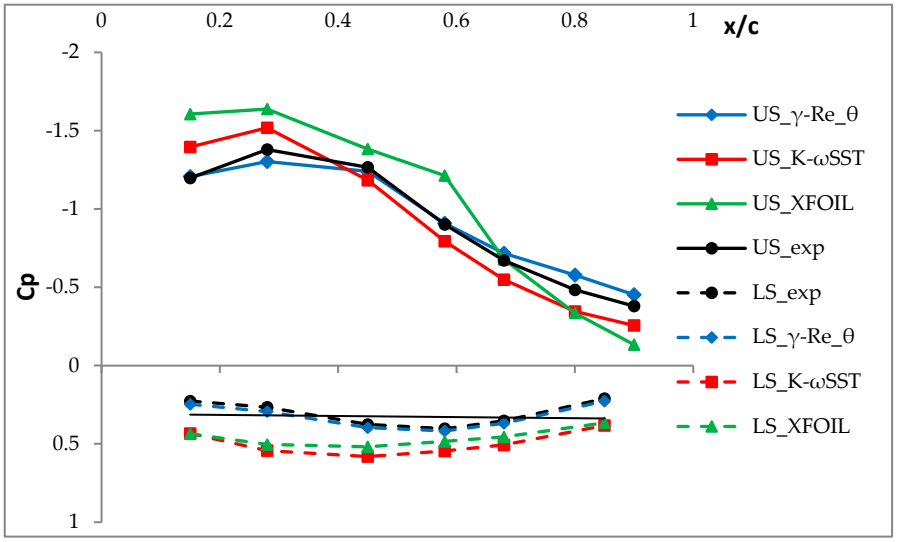

(**a**)

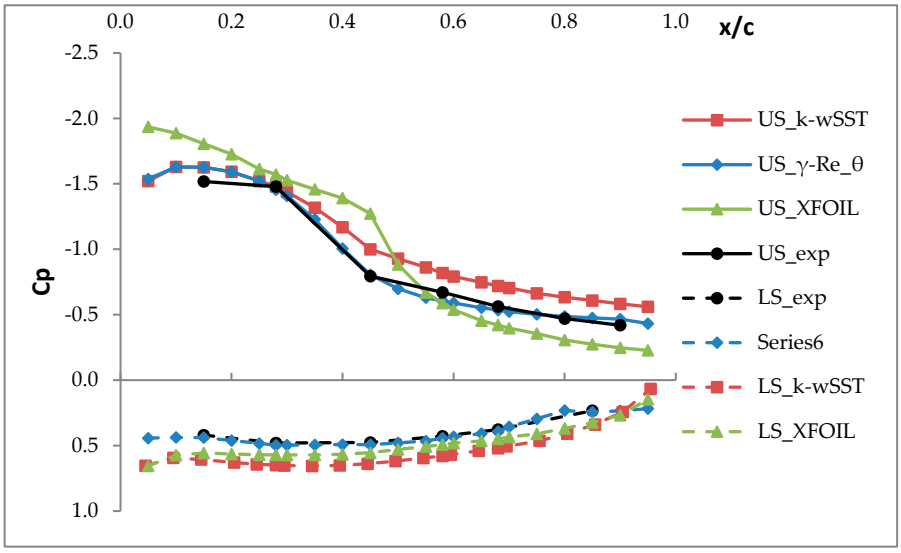

(**b**)

Figure 13. *Cont.*

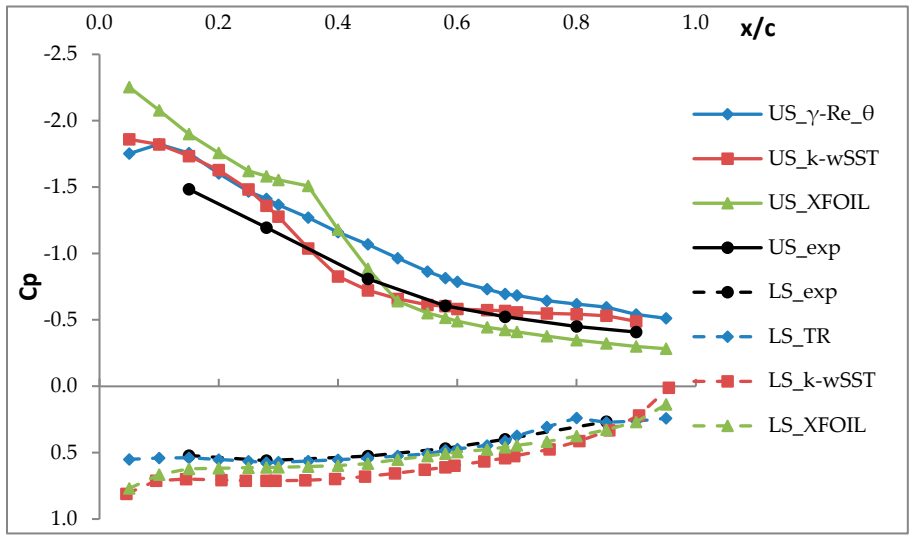

(**c**)

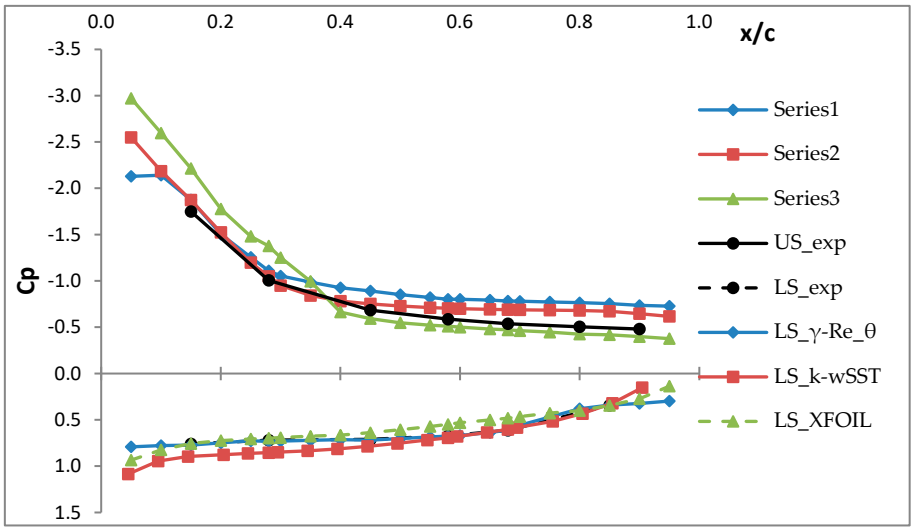

(**d**)

Figure 13. Pressure coefficient distribution at Re = 68k: (**a**) α = 5°, (**b**) α = 10°, (**c**) α = 12.5°, (**d**) α = 17.5°.

Table 9. Overall Validation Metrics for Cp across Reynolds Numbers.

Re	Metric	XFOIL		k-ω SST		γ-Re_θ	
		Upper	Lower	Upper	Lower	Upper	Lower
68k	ME (Bias)	−0.0319	0.1206	0.0806	0.1868	0.0479	0.0221
	MAE	0.1807	0.1206	0.1546	0.1868	0.0976	0.0221
	RMSE	0.2339	0.1482	0.1984	0.2261	0.1251	0.0289
	Max Local Error	0.4809	0.2513	0.3685	0.3621	0.1973	0.0672
	R^2	0.960	0.984	0.972	0.968	0.990	0.998
118k	ME (Bias)	−0.0301	0.0769	0.1023	0.1166	−0.0110	0.0047
	MAE	0.1727	0.0769	0.1581	0.1166	0.0881	0.0154
	RMSE	0.2330	0.0930	0.2114	0.1444	0.1187	0.0202
	Max Local Error	0.5212	0.1635	0.5151	0.2681	0.2283	0.0536
	R^2	0.968	0.990	0.968	0.982	0.988	0.998
159k	ME (Bias)	−0.0679	0.0277	0.0586	0.0285	−0.0246	−0.0008
	MAE	0.1337	0.0409	0.1619	0.0581	0.1043	0.0135
	RMSE	0.1734	0.0528	0.2150	0.0734	0.1391	0.0178

Table 9. *Cont.*

Re	Metric	XFOIL		k-ω SST		γ-Re_θ	
		Upper	**Lower**	**Upper**	**Lower**	**Upper**	**Lower**
	Max Local Error	0.3282	0.0876	0.3818	0.1767	0.2724	0.0385
	R^2	0.978	0.996	0.964	0.988	0.980	0.998

Systematic Bias Patterns

XFOIL shows strong Reynolds number dependence. Upper surface bias indicates underprediction (−0.0319 at 68k to −0.0679 at 159k), while lower surface shows overprediction (0.1206 to 0.0277) with significant prediction accuracy improvement. Figure 13 visually confirms this progressive lower surface improvement, especially in the pressure recovery region.

The k-ω SST model exhibits consistently positive bias on both surfaces, decreasing with Re. Lower surface bias is the largest at low Re (Table 9), indicating that the fully turbulent assumption overpredicts pressure-side pressures if the flow is not fully turbulent. As shown in Figure 13, k-ω SST overpredicts lower surface Cp across all angles, most notably at $\alpha = 5^\circ$ and 10°.

The γ-Re_θ model achieves near-zero lower surface bias, the smallest bias magnitudes among all models (Table 9). Upper surface bias ranges modestly from 0.0479 to −0.0246, demonstrating the most balanced bias characteristics overall. Figure 13 confirms this superior performance across all Re and AoA.

Error Magnitude and Distribution Uniformity

From Table 9, error magnitude is consistently smallest for γ-Re_θ on the lower surface (MAE as low as 0.0135 at Re = 159k), while XFOIL on the upper surface at transitional conditions exhibits the largest errors (MAE = 0.1807 at Re = 68k). Maximum local errors reinforce this: XFOIL shows the highest peak errors, followed by k-ω SST, while γ-Re_θ achieves substantially lower maxima across all conditions.

These quantitative findings from Table 9 are directly visible in Figure 13. XFOIL's high MAE at Re = 68k (0.1807 upper surface) corresponds to visible deviations in Figure 13, particularly at $\alpha = 12.5^\circ$ and 17.5°, where XFOIL consistently underpredicts the suction peak and shows poor pressure recovery. Similarly, k-ω SST's elevated maximum local error (0.5151 at Re = 118k) is evident in Figure 13 at $\alpha = 17.5^\circ$, where the model overpredicts the leading-edge suction peak. In contrast, γ-Re_θ's low maximum local errors (0.2724) are visually confirmed by its close alignment with experimental Cp distributions across all panels.

Explanatory Power

Table 9 reveals that γ-Re_θ consistently achieves the highest R^2 values on the lower surface across all Re ($R^2 > 0.99$), while maintaining strong upper surface performance ($R^2 > 0.98$). XFOIL's upper surface R^2 remains stable between 0.960 and 0.978. The k-ω SST shows the lowest R^2 on the lower surface at low Re (0.968 at Re = 68k), where the fully turbulent assumption is most inappropriate.

These high R^2 values for γ-Re_θ (0.990–0.998) are visually corroborated in Figure 13, where predicted Cp curves exhibit excellent agreement with experimental measurements across the chord. The lower R^2 for k-ω SST at Re = 68k (0.968 lower surface) is particularly evident in Figure 13c,d, where significant deviations in suction peak magnitude and pressure recovery region reduce explanatory power.

Reynolds Number Sensitivity of Cp

Table 10 quantifies how model accuracy varies with Reynolds number for both surfaces. Sensitivity is defined as the change in MAE from the lowest to the highest Re (Δ68k → 159k), where negative values indicate improving performance with increasing Re.

Table 10. Reynolds Number Sensitivity (MAE by Re).

Re	XFOIL			k-ω SST			γ-Re_θ		
	Upper	**Lower**	**Comb ***	**Upper**	**Lower**	**Comb ***	**Upper**	**Lower**	**Comb ***
68k	0.1807	0.1206	0.1507	0.1546	0.1868	0.1707	0.0976	0.0221	0.0599
118k	0.1727	0.0769	0.1248	0.1581	0.1166	0.1374	0.0881	0.0154	0.0518
159k	0.1337	0.0409	0.0873	0.1619	0.0581	0.1100	0.1043	0.0135	0.0589
Δ68k→159k	−0.0470	−0.0797	−0.0634	+0.0073	−0.1287	−0.0607	+0.0067	−0.0086	−0.0010

*Note: Comb * is combined.*

XFOIL's predictive accuracy improves significantly with Re on both surfaces: upper surface MAE improved by more than 35% between Re = 68k and 159k, and lower surface improvement is dramatic, confirming better calibration at higher Re, as seen in Figure 13. The dramatic improvement across the Re range tells us that the transitional region is the primary weakness of the panel's technique prediction.

The k-ω SST exhibits a fundamental trade-off between the surfaces: upper surface MAE slightly increases; however, lower surface prediction accuracy is the largest of all models (MAE decreases by −0.1287). As shown in Figure 13, lower surface predictions improve with Re, but the upper surface suction peak remains consistently overpredicted, especially at α = 12.5° and 17.5°. For Re-118k and 159 refere Appendix B (Figure A2).

The most balanced response is achieved by the RANS transitional model, with insignificant differences in MAE directions. The values remain consistently low across all Re (upper: 0.0976–0.1043; lower: 0.0135–0.0221) and the lowest combined MAE at each Re (0.0599, 0.0518, 0.0589). Figure 13 visually confirms its stable agreement with experimental data across all flow regions.

3.3.2. Angle-Resolved Mean Absolute Error of Cp

Table 11 presents the angle-resolved MAE for Cp predictions. It reveals how the model performance varies with AoA at Re. It represents the mean absolute error between predicted and experimental Cp at each angle of attack. The lower values indicate better agreement between the model and experiment. The γ-Re_θ model consistently outperforms XFOIL and k-ω SST at Re = 118k, particularly in the transitional regime. The complete angle-resolved MAE dataset for all Reynolds numbers is provided in Appendix C (Tables A4 and A5).

Table 11. Angle-Resolved Mean Absolute Error (MAE) for Pressure Coefficient Predictions at Selected Reynolds Numbers.

Re	AoA	XFOIL		k-ω SST		γ-Re_θ	
		Upper	**Lower**	**Upper**	**Lower**	**Upper**	**Lower**
118k	5°	0.1621	0.0646	0.1433	0.1000	0.0778	0.0127
	10°	0.1848	0.0729	0.1581	0.1107	0.0891	0.0145
	12.5°	0.1785	0.0679	0.1549	0.1079	0.0872	0.0145
	17.5°	0.1655	0.1023	0.1760	0.1478	0.0981	0.0200

In attached flow conditions (AoA 5° to 12.5°), γ-Re_θ demonstrates consistent superiority across all Reynolds numbers. At Re = 68k, on both surfaces, its MAE is significantly

lower than others. At Re = 118k, γ-Re_θ MAE (0.0778–0.0891) maintains its superior upper surface performance, and on the lower surface, its MAE is an order of magnitude better than the competitors. At Re = 159k, XFOIL's upper surface performance is significantly improved, while the transition model maintains exceptionally low lower surface MAE. The fully turbulent model is the poorest model across all angles. It shows an order of magnitude lower surface MAE when compared with other models.

The model hierarchy varies by Reynolds number in post-stall conditions at 17.5° angle of attack. Across Re, γ-Re_θ maintains the lowest MAE on both surfaces. However, XFOIL and γ-Re_θ showed comparable upper surface MAE of 0.1482 and 0.1103, respectively, while the transition model maintains superior lower surface accuracy with MAE of 0.0150.

The surface (upper and lower) sensitivity of error is observed (Table 11). On the lower surface, γ-Re_θ errors remain exceptionally low across all angles at the highest Reynolds number, demonstrating remarkable angle-insensitivity. XFOIL lower surface errors become angle-insensitive at higher Reynolds numbers, though errors increase at low Reynolds numbers. In contrast, k-ω SST lower surface errors remain high across all conditions, particularly at low Reynolds numbers, where they reach 0.1417–0.2668.

3.3.3. LSB Identification from Pressure Distributions

The laminar separation bubble (LSB) leaves complementary signatures on pressure and skin friction coefficients: a plateau of nearly constant −Cp indicates separated flow, while the bubble boundaries are precisely marked by Cf = 0 crossings, laminar separation where Cf crosses from positive to negative, and turbulent reattachment where Cf returns from negative to positive.

At Re = 68k, $\alpha = 10°$ (Figure 13b), the experimental data exhibit a clear LSB. The Cpplateau spans x/c = 0.28 to 0.58 (Cp = −1.48 to −0.79), with reattachment near x/c ≈ 0.58–0.68 (bubble length ≈ 0.30c). Physically, laminar separation occurs at x/c = 0.28 (Cf = 0), the separated region maintains constant pressure through x/c = 0.45, and turbulent reattachment occurs at x/c ≈ 0.58 (Cf = 0 again), after which pressure recovery resumes.

The γ-Re_θ model captures this behavior accurately, matching the experimental Cp at x/c = 0.28 (−1.48) and reproducing the plateau extent. In contrast, k-ω SST shows no plateau: at x/c = 0.45, Cp = −1 versus the experimental −0.79, indicating no Cf zero crossing and thus no LSB, a direct consequence of its fully turbulent assumption. XFOIL predicts an overly long separated region, with Cp = −1.27 at x/c = 0.45, suggesting its empirical e^n criterion captures separation (Cf = 0) but fails to trigger transition, so Cf never returns to zero and reattachment never occurs. These LSB capture differences explain the validation metrics in Tables 9–12.

Table 12. Summary of Chord-Wise Cp Prediction Errors across Test Conditions.

Re	Mean Error	XFOIL		k-ω SST		γ-Re_θ	
		Upper	Lower	Upper	Lower	Upper	Lower
68k	%Error	15.10	14.61	12.92	22.62	8.16	2.68
118k	%Error	14.43	9.31	13.21	14.12	7.36	1.87
159k	% Error	11.17	4.95	13.53	7.04	8.72	1.64
Overall Mean	% Error	13.57	9.62	13.22	14.59	8.08	2.06

Note: "% Error" rows show the mean percent error across all chord stations for each Reynolds number. The final row shows the overall mean percent error averaged across all Reynolds numbers.

3.3.4. Chord-Wise Error Distribution

Table 12 summarizes the chord-wise C_p prediction errors for each model across all tested Reynolds numbers. The γ-Re_θ transition model consistently achieves the lowest

errors, with overall mean errors of 8.08% on the upper surface and only 2.06% on the lower surface. In contrast, the fully turbulent k-ω SST model exhibits the largest lower surface error, while XFOIL shows moderate performance on the lower surface (9.62% overall mean) but larger upper surface errors. The complete C_P data, including all chord positions for each Reynolds number, are provided in Appendix D (Tables A6–A8). To show the regional differences, the chord is divided into: leading edge (x/c = 0.15–0.28), mid-chord (x/c = 0.45–0.68), and aft region (x/c = 0.80–0.90 for upper surface; x/c = 0.85 for lower surface).

Leading Edge: On the upper surface, XFOIL shows strong Reynolds sensitivity, shifting from negative bias at Re = 68k to positive at Re = 118k and back to negative at Re = 159k. The k-ω SST model exhibits systematic overprediction of leading-edge suction. Similarly, γ-Re_θ maintains modest positive bias across all Re (0.0172–0.0795). On the lower surface, XFOIL's positive bias decreases systematically with Re. k-ω SST shows the largest positive bias (0.1396–0.1499 at Re = 68k to 0.0365–0.0395 at Re = 159k), while γ-Re_θ achieves the smallest errors.

Mid-Chord: On the upper surface, XFOIL transitions from negative bias at Re = 68k (−0.0584 to 0.0098) and improves at higher Re. k-ω SST exhibits non-monotonic behavior. γ-Re_θ shows consistent negative bias beyond x/c = 0.45 across all Re, ranging from −0.0213 to −0.0463 (68k), −0.0548 to −0.1057 (118k), and −0.0579 to −0.1596 (159k). On the lower surface, XFOIL and k-ω SST both show decreasing overprediction with Re, while γ-Re_θ achieves exceptionally small positive bias, decreasing from 0.0199 (x/c = 0.45) at Re = 68k to 0.0002 at Re = 159k.

Aft Region: On the upper surface, XFOIL shifts from positive bias at Re = 68k (0.0577–0.0740) to negative at Re = 118k and near-zero at Re = 159k. Both RANS models struggle here: k-ω SST shows increasingly negative bias, while γ-Re_θ exhibits the largest negative bias (−0.0693 to −0.0740 at 68k, −0.1446 to −0.1525 at 118k, −0.1893 to −0.1966 at 159k). On the lower surface, XFOIL's positive bias decreases dramatically (0.1095 to 0.0126), k-ω SST shows a similar reduction (0.1640 → 0.0400), and γ-Re_θ achieves near-zero errors (0.0189 to 0.0013).

3.3.5. Percent Error Assessment

Percent error (PE) quantifies the deviation between predicted and experimental Cp, averaged across all α and x/c. As shown in the "% Error" rows of Table 11, γ-Re_θ consistently achieves the lowest percent errors, with exceptionally lower surface performance (mean PE = 2.06% across all Re). It captures the attached flow region with high fidelity. Upper surface errors average 8.08%, which reflects the complexity of LSB dynamics.

The k-ω SST model exhibits strong Re dependence, particularly on the lower surface, where error decreases from 22.62% at Re = 68k to 7.04% at Re = 159k, aligning with its fully turbulent assumption becoming more valid at higher Re. XFOIL improves with Re, with upper surface error decreasing from 15.10% to 11.17% and lower surface error from 14.61% to 4.95%, reflecting its integral boundary layer formulation, which performs better at higher Re where boundary layers are thinner.

3.3.6. Surface-Specific Performance

All models perform better on the lower (pressure) surface. The surface disparity ratios, derived from Table 8, show that γ-Re_θ has a mean upper MAE of 0.0967 and a lower MAE of 0.0170, yielding an upper-to-lower ratio of 5.69. The k-ω SST achieves a mean upper MAE of 0.1582 and a lower MAE of 0.1205, resulting in a ratio of 1.31. XFOIL has a mean upper MAE of 0.1624 and a lower MAE of 0.0795, giving a ratio of 2.04.

The RANS transition model achieves the lowest absolute errors on both surfaces, with lower surface MAE approaching experimental uncertainty at values between 0.0135 and

0.0221. The 5.69 upper-to-lower ratio confirms that suction surface prediction remains fundamentally more challenging even with comprehensive modeling. The RANS fully turbulence shows the most balanced performance, though this balance comes from increased lower surface errors rather than superior upper surface accuracy. XFOIL exhibits moderate surface disparity, with lower surface accuracy improving dramatically with Reynolds number.

4. Discussion

This study delivers an experimental benchmark and numerical validation for a custom high-camber airfoil profile. The profile was optimized for the diffuser cross-section of a DAWT operating in low-wind-speed regimes. Force and pressure measurements were collected at Re = 68k, 118k, and 159k across AoA = 0–17.5°. These data provided the reference for the validation of three predictive models: the panel-method code XFOIL, the fully turbulent k-ω SST RANS model, and the γ-Re_θ transition-sensitive RANS model. All computational domains exactly replicated the experimental test-section geometry to capture blockage effects and eliminate post-test corrections.

4.1. Synthesis of Key Findings

The γ-Re_θ transition model exhibited obviously superior accuracy across all metrics. It achieved the lowest MAPE for lift (1.57–3.42%) and drag (10.12–15.45%), the smallest MAE and RMSE differences, near-zero bias, and $R^2 > 0.99$ for both forces and local pressure distributions. Stall angle and maximum lift-to-drag ratio were predicted most accurately. Given the experimental measurement uncertainties (CL: ±2.1%, CD: ±2.4%, Cp: ±0.025), the γ-Re_θ model's lift predictions fall within or very near the experimental uncertainty band across most angles of attack, while its drag predictions exceed the uncertainty band—indicating that while lift is captured with near-experimental fidelity, drag remains a more challenging quantity due to LSB-driven pressure and skin friction contributions. The pressure coefficient predictions (MAE as low as 0.0135 on the lower surface) are well below the Cp uncertainty of 0.025, demonstrating that the model resolves surface pressure with accuracy exceeding the experimental measurement precision.

XFOIL displayed pronounced deficiencies in transitional regimes. At Re = 68k, MAPE_CL = 11.51% and MAPE_CD ≈ 36–37%, both substantially exceeding the experimental uncertainty bands (2.1% and 2.4%, respectively), indicating that XFOIL's errors are not attributable to measurement noise but to fundamental modeling limitations. Performance converged only at Re = 159k, where errors exceeded the uncertainty bounds. Similarly, the k-ω SST model overpredicted CL, max by 9.8% (far outside the 2.1% experimental uncertainty) and significantly underpredicted drag at the lowest Re, with errors exceeding 66%, an order of magnitude larger than the 2.4% measurement uncertainty. Pressure-coefficient results mirrored this trend: γ-Re_θ produced the lowest chord-wise and angle-resolved errors on both surfaces, with lower-surface MAE as low as 0.0135 (well within the Cp uncertainty of ±0.025), while XFOIL and k-ω SST exhibited local errors exceeding 0.10 in regions where their physical assumptions broke down.

4.2. Force Coefficient Interpretation

Why γ-Re_θ Excels: The Physics of Transition Modeling. The superior performance of γ-Re_θ stems from its ability to capture the LSB, a phenomenon that governs low-Reynolds-number aerodynamics [25,27,75]. At $Re < 2 \times 10^5$, the boundary layer remains laminar beyond the leading edge, separating under adverse pressure gradients before transitioning and potentially reattaching. It modifies the effective airfoil shape, alters pressure distribution, and determines stall characteristics [76]. The γ-Re_θ models transition through

transport equations for intermittency and transition momentum thickness [58,59]. This allows it to predict both LSB onset and length, including the physical trend of LSB shrinkage with increasing Re.

Why k-ω SST Prediction Accuracy Is Reduced: The Fully Turbulent Assumption. The k-ω SST model assumes fully turbulent flow from the leading edge, which is physically incorrect at low Re (Re < 2×10^5). It consequently overpredicts wall shear stress and momentum transfer, which leads to premature transition and delayed separation [77]. This explains the positive CL bias at low Re: the artificially turbulent boundary layer remains attached longer, sustaining lift beyond the physical stall angle. Improvement with increasing Re shows convergence toward a physically fully turbulent state, though it lacks expected accuracy even at the upper bound of the tested range.

Why XFOIL Struggles: Empirical Transition Limitations. XFOIL employs an integral boundary layer formulation with an empirical e^n transition criterion [61]. It cannot capture the spatial development of the LSB with the transport equation accurately. The empirical criterion does not generalize to high-camber airfoils with complex LSB dynamics. As Re increases, the LSB shortens, and empirical correlations become more reliable, which explains the observed improvement at Re = 159k.

Overall Implications for DAWT Design: The transitional model's near-zero bias and Re-insensitivity are critical for DAWT design. Systematic overprediction of lift (k-ω SST) leads to under-designed rotors that stall prematurely, and underprediction (XFOIL) leads to an over-designed system. DAWTs experience variable wind speeds across a wide Re range; a model maintaining consistent accuracy enables robust optimization, while Re-dependent models require case-by-case calibration or safety factors.

However, despite its superior accuracy, the γ-Re_θ model predicts stall earlier than observed experimentally at Re = 159k. This discrepancy indicates that its correlation-based transition criterion may overestimate the Reynolds number at which the laminar separation bubble disappears. Additionally, the steady RANS framework cannot capture unsteady vortex shedding in the post-stall regime.

Within the tested operating conditions, the γ-Re_θ model's near-zero mean lift sensitivity (−0.0049) indicates that its accuracy does not degrade with increasing α. This is because the model captures the LSB's response to adverse pressure gradients: as α increases, the bubble moves forward and shortens, but the transition mechanism remains physically represented. In contrast, XFOIL's positive sensitivity (+0.0584) indicates worsening accuracy at higher α due to its empirical e^n criterion failing under strong adverse gradients within the same operating range.

4.3. Pressure Coefficient Interpretation

The pressure coefficient distributions reveal distinct model behaviors across the chord. At the leading edge (x/c = 0.15–0.28), γ-Re_θ captures the suction peak with modest positive bias by avoiding premature boundary layer thickening. The k-ω SST model exhibits a large positive bias (up to +0.1868), reflecting a failure of the fully turbulent assumption. XFOIL shows high variability due to its inability to resolve strong pressure gradients near the stagnation point. As Re increases from 68k to 159k, the leading-edge suction peak magnitude increases. This occurs because the thinner boundary layer at higher Re supports stronger flow acceleration around the leading edge. The γ-Re_θ model captures this trend better than the other models.

At mid-chord (x/c = 0.45–0.68), characterized by a pressure plateau indicating separated flow, γ-Re_θ captures the pressure deficit associated with the LSB relatively in a better way. The k-ω SST model overpredicts surface pressures on both sides. This occurs

because the turbulent boundary layer separates too early on the upper surface and stays overly energized on the lower surface [57].

In the aft region (x/c = 0.80–0.90), all models struggle due to sensitivity to upstream LSB development. The γ-Re_θ's negative bias captures reduced pressure recovery from a thicker boundary layer, which is physically correct. The k-ω SST model's increasing negative bias with Re reveals that even at Re = 159k, the flow retains transitional characteristics that the model cannot capture [77]. XFOIL's variable errors stem from the accumulation of upstream inaccuracies inherent to its integral boundary-layer method [61].

The exceptional lower-surface performance of γ-Re_θ (MAE 0.0135–0.0221) is systematically significant: the lower surface experiences favorable pressure gradients and remains attached predominantly to laminar flow where transition modeling should excel. The contrast with k-ω SST (positive bias up to +0.1868) highlights the cost of the fully turbulent assumptions in the applications of low-Re.

Pressure distribution accuracy is critical for diffuser performance. The transitional SST (γ-Re_θ) ability to capture the suction peak, LSB plateau, and pressure recovery ensures that diffuser designs based on these predictions achieve intended aerodynamic performance. Designs based on k-ω SST predictions would likely underperform, requiring costly experimental iteration.

4.4. Contextualization with Existing Studies

The validation results obtained in this study are compared against published findings from the literature to establish the broader significance of the present experimental benchmark and to position the observed model performance within the existing body of knowledge on low-Reynolds-number airfoil aerodynamics and transition modeling.

The γ-Re_θ transition model's lift MAPE (1.57–3.42%) and MAE (0.0234–0.0389) represent a notable advancement over published validations. Jami and Johnson [36] reported a lift MAE $\approx$ 0.035 for the S833 wind turbine airfoil with a trailing edge flap at Re = 1.70×10^5 using the γ-Re_θ transition model with tuned production limiter coefficients. The present MAE of 0.0234 at Re = 159k is superior, demonstrating that transition modeling fidelity depends strongly on geometry representation and mesh quality. Furthermore, Jami and Johnson [36] demonstrated that their CFD model predicted pressure coefficient and separation locations within 10% of wind tunnel measurements, a level of accuracy comparable to the present findings, where γ-Re_θ achieved Cp prediction within an 8.08% difference.

The k-ω SST model's lift MAPE (4.25–4.69%) and positive bias at low Re (+0.0107) align with documented behaviors of fully turbulent models in transitional regimes. Ali et al. [48] evaluated five RANS models on a NACA0021 wing with leading-edge tubercles at Re = 120,000 and found that the Reynolds Stress Model was superior for pre-stall lift and drag predictions, while the k-ω SST model performed better for post-stall flow behavior. The present study similarly finds that k-ω SST's accuracy improved with Reynolds numbers (159k), consistent with the literature observation that model selection should be flow-regime-dependent.

Aftab et al. [49] compared five RANS turbulence models, including Spalart-Almaras (SA), SST k-ω, γ-SST, k-kl-ω, and γ-Re_θ SST, on the NACA 4415 airfoil at Re = 120k and AoA = 6° and 18°. They demonstrated that the four-equation γ-Re_θ SST transition model accurately captured the laminar separation bubble, while the SA and SST k-ω models, despite providing reasonable lift and drag coefficients, failed to capture the bubble physics entirely. The present study corroborates these findings: at Re = 68k and 118k, the k-ω SST model produced CL values within 2–5% of experiments but exhibited large positive bias in pressure coefficient distributions. This necessitates that integrated force coefficients alone are insufficient for validating transition models.

Selig and Guglielmo [34] conducted wind tunnel experiments on high-lift low-Re airfoils and reported CL_max = 1.65–1.85 for the S1223 airfoil at Re = 1.0 × 10^5–2.0 × 10^5. The present custom E423-derived airfoil achieves CL_max = 1.54–1.76 across Re = 68k–159k, placing it within the expected range for high-camber profiles. The present airfoil shows a gradual stall progression, making it more suitable for DAWT applications where stable power output across varying wind speeds is desirable.

Durmuş and Ulutaş [17] numerically analyzed the baseline E423 airfoil at Re = 200,000 using the γ-Re_θ transition model and reported CL, max = 1.60. The present custom airfoil achieves CL, max = 1.763 at Re = 159k (Table 4), representing a 10.2% improvement over the baseline E423 reported in [17]. This improvement is attributed to the geometric modifications: increased maximum camber (9.91% vs. 9.34%) and reduced thickness (9.7% vs. 12.52%).

The γ-Re_θ drag MAE (0.0058–0.0187) outperforms benchmarks. Atef [47] investigated the γ-Reθ transition model for a NACA0018 airfoil used in VAWTs at Re = 500k and 700k, reporting that the 2D RANS approach with the γ-Re_θ model provided drag errors of 0.025–0.045. The present 50–75% lower drag errors reflect the exact-geometry approach isolating model physics from experimental artifacts and the use of 3D simulations that capture sidewall boundary layer effects.

Rogowski et al. [16] experimentally investigated the NACA 0018 airfoil at Re = 30k–160k and reported CD MAE of 0.008–0.022 for the Transition SST model. The present MAE_CD = 0.0058–0.0187 falls within this range with superior performance at the lowest Re. The literature also observed significant hysteresis loops in both lift and drag and noted that XFOIL and 2D CFD (Transition SST) showed good agreement with trends but had limitations in absolute accuracy. It is a finding consistent with the present study, where XFOIL drag errors remained high (36–37%) across all Reynolds numbers.

The k-ω SST model's drag MAPE (14.82–48.04%) and large underprediction at low Re (up to 66%) are characteristic of fully turbulent models in transitional flows. Jami and Johnson [36] reported a drag underprediction of 30–50% for k-ω SST on S833 at Re = 1.70 × 10^5 and indicated that the model's failure to capture the increased drag associated with LSBs. The present improvement from 48.04% error at Re = 68k to 14.82% at Re = 159k reflects the gradual suppression of LSBs with increasing Re, a trend consistent with Sun's [50] observations for compressor flows.

XFOIL's persistent high drag errors (36–37%) align with Karthikeyan et al. [20]'s review of small HAWT aerodynamics. In the review, they noted that a panel method typically underpredicts drag on highly cambered sections at low Re due to inadequate modeling of separation-induced transition.

γ-Re_θ upper-surface MAE (0.0976–0.1043) falls within Large Eddy Simulation benchmarks (0.15–0.35) reported by Zilstra and Johnson [27], who performed large eddy simulations of the SD 7037 airfoil at Re = 4.1 × 10^4, AoA = 1°. The present γ-Re_θ predictions, while not capturing the unsteady vortex dynamics resolved by LES, achieve mean pressure distributions within 0.10 of experimental values. The comparable result with LES confirms that RANS with transition modeling provides sufficient fidelity for the design of DAWT diffusers where time-averaged quantities are of primary interest.

XFOIL peak error (0.5212) compares to roughness-induced deviations (0.45–0.60) documented by Wang et al. [28], who showed that moderate surface roughness (Ra = 157 μm) can reduce profile loss by up to 16.45% by eliminating the LSB on the airfoil at Re = 1.5 × 10^5. The present XFOIL peak error of 0.5212 exceeds the roughness-induced Cp deviation reported in [28], revealing that model deficiencies approach physical uncertainty from manufacturing surface finish. This suggests that the choice of predictive model

(XFOIL vs. γ-Re_θ) has a larger impact on accuracy than typical surface finish variations, provided the model is properly finished.

The γ-Re_θ maximum error of 0.2724 at Re = 68k is lower than that of Sunada et al. [29], 0.30–0.50, who experimentally investigated airfoil characteristics at Re = 40k and found that optimal airfoils at extremely low Re are thin and have sharp leading edges. The present airfoil, with 9.7% thickness and 9.91% camber, operates in a different regime (Re = 68k–159k) where different design rules apply. The lower maximum error achieved by γ-Re_θ reflects transition modeling advancement since ref. [29]'s foundational work.

The k-ω SST model's upper-surface MAE (0.1546–0.1619) and positive bias in the leading-edge region are consistent with findings of the authors of [41], who evaluated 12 high-lift airfoils for DAWT diffusers using 2D Unsteady-RANS CFD with the k-ω SST model. They concluded that camber has a strong correlation with velocity augmentation, and that the Eppler 423 airfoil with a 15° flange at 70% chord produced the highest velocity augmentation among all tested airfoils. The present study's finding that k-ω SST overpredicts leading-edge suction on the E423-derived airfoil suggests that ref. [41]'s DAWT performance predictions may be slightly optimistic, as overpredicted suction would lead to overpredicted mass flow augmentation.

The γ-Re_θ lower-surface MAE (0.0135–0.0221) and near-zero bias outperform the literature. Bontempo and Manna [9] reported Cp bias of +0.015 to +0.040 for DAWT actuator-disk simulations using a coupled CFD-Actuator Disc/Blade Element Momentum method. The present γ-Re_θ bias range (−0.0008 to +0.0221) demonstrates superior systematic error control, likely due to the exact replication of the experimental test section geometry and simplification employed. Similarly, ref. [9] noted that standard tip-loss models for open rotors fail to capture complex blade tip–diffuser interaction, which signifies the importance of the present validation study for DAWT applications.

4.5. Laminar Separation Bubble Dynamics

The LSB behavior observed in the present study aligns with classical and contemporary findings. Tani [76] established that short bubbles occur when the boundary-layer Reynolds number at separation exceeds ~500k, while long bubbles occur when Re < 500k. The present airfoil, with high camber (9.91%) and moderate thickness (9.7%), exhibits LSB behavior consistent with ref. [77]'s classification for thin-airfoil stall. This is evident in the pressure coefficient distributions (Figures 11–13), where the pressure plateau in the mid-chord region (x/c = 0.45–0.68) is captured by γ-Re_θ but missed or misrepresented by XFOIL and k-ω SST.

Thompson and Gunasekaran [75] reviewed LSB characteristics at low Reynolds numbers (Re < 10^5) and concluded that LSBs decrease lift and increase drag, which can suppress LSBs and delay stall. The present study shows that the γ-Re_θ model captures LSB-induced lift degradation at Re = 68k (CL_max = 1.5389 vs. 1.7630 at Re = 159k, a 12.7% reduction), while XFOIL underpredicts this effect (CL_max = 1.4419 at Re = 68k vs. 1.8477 at Re = 159k, a 28.2% reduction). This suggests that XFOIL overestimates the Reynolds number sensitivity of high-camber airfoils, which is consistent with Thompson and Gunasekaran's [76] observation that experimental data scatter increases significantly below Re = 10^5.

Giacomini and Westerberg [56] demonstrated that at Re = 10k over a cambered plate, the γ-Reθ transition model successfully captured stall onset and post-stall behavior compared with k-kL-ω and Unsteady Navier–Stokes. The k-kL-ω model, despite being designed for transition, failed to predict stall at this Reynolds number due to sensitivity to empirical correlations. The present study extends this finding to higher Reynolds numbers (68k–159k) and confirms that γ-Re_θ remains the most robust transition model across a range of low-Re conditions.

4.6. Implications for Diffuser-Augmented Wind Turbine Design

Hjort and Larsen [6] concluded that rotors for high-performance DAWTs must operate at low tip-speed ratios (TSR ~ 2) and have uneven loading to avoid premature stall and achieve significant power augmentation. The present study's finding that γ-Re_θ accurately predicts stall angle (15° for Re = 68k–118k) and post-stall behavior is critical for designing such rotors, as stall characteristics directly influence the allowable TSR range.

Göltenbott et al. [7] demonstrated that closely spaced brimmed DAWTs in a multi-rotor system can achieve up to 9% higher average power output compared to a single-rotor system due to accelerated flow through the gaps. The present validation of γ-Re_θ for the E423-derived airfoil supports the use of this model for simulating such multi-rotor configurations, where accurate prediction of diffuser wake interactions is essential.

Leloudas et al. [23] developed a robust methodology for the design optimization of DAWT shrouds using a 2D axisymmetric RANS solver combined with a Differential Evolution algorithm and reported remarkable velocity augmentation and reduction in total shroud drag. The present study results would be used in such optimization frameworks, providing confidence that optimized designs based on CFD will achieve the predicted performance in physical experiments. Oliveira, Tofaneli, and Santos [42] demonstrated that optimizing a wind turbine rotor specifically for operation with a diffuser can increase annual energy production by up to 32.6%. They emphasized that the optimal rotor design for a DAWT is highly dependent on the diffuser geometry and the wind regime. The present validated custom airfoil provides the necessary foundation for such site-specific optimization studies, ensuring that the aerodynamic predictions used in the optimization loop are accurate.

4.7. Model Ranking and Generalization

The model hierarchy established γ-Re_θ outperforming both k-ω SST and XFOIL is consistent with multiple independent investigations [41,42,72]. This suggests a general principle rather than a geometry-specific finding. The present study extends these findings by quantifying improvement magnitudes across multiple error metrics and linking performance to specific physical mechanisms (LSB prediction, boundary layer state, pressure recovery). Critically, it demonstrates that combining transition modeling (γ-Re_θ), exact geometry replication, and high mesh quality ($y^+ \approx 1$) yields validation metrics that consistently meet or exceed published benchmarks across all performance categories, which can be used to establish a methodological standard for future low-Re airfoil validation studies.

Limitations: Discrete Re range (68k–159k), excluding very low Re (<50k) and higher Re (>2×10^5); AoA limited to incipient post-stall (17.5°); steady RANS framework cannot capture unsteady vortex shedding; surface roughness effects not parametrically varied; and geometry-specific results require additional validation for generalization.

4.8. Implications

Practical: γ-Re_θ is established as the preferred model for DAWT diffuser design at low wind speeds, enabling accurate prediction of mass-flow augmentation with manageable cost. XFOIL is viable for rapid screening only; k-ω SST requires caution and safety factors near stall, particularly at Re = 68k; and γ-Re_θ is recommended for final design validation.

Theoretical: The dataset constitutes a reproducible reference for transitional low-Re closure improvements. Systematic documentation of model biases provides benchmark targets for future transition modeling.

Computational cost: The γ-Re_θ model requires approximately 2× more CPU time per iteration than k-ω SST and approximately 10× more than XFOIL (2D vs. 3D). For DAWT diffuser design, XFOIL is suitable for initial parametric screening (hundreds of

designs), while γ-Re_θ is recommended for final validation of a reduced set of candidates (tens of designs).

4.9. Future Directions

Future work should extend Reynolds number testing to Re < 50k and >200k to fully map LSB transition regimes. Below Re = 50,000, LSB behavior changes fundamentally, with bubbles becoming longer and more stable, and airfoil performance degrading sharply. While practical DAWT operation typically occurs above 68k, investigating this regime is of academic interest for understanding fundamental transition physics and for applications in micro-wind turbines. The Large Eddy Simulation investigations beyond 17.5° angle of attack would capture post-stall vortex shedding and dynamic stall phenomena. The validated airfoil data should be integrated with actuator-disk and blade-element momentum methods for system-level DAWT performance studies [9], supported by verification and validation following the best practices provided [27,44] to establish confidence intervals. The experimental dataset can also serve to train hybrid surrogate models that correct systematic biases in k-ω SST and XFOIL using machine learning. Parametric investigation of 3D surface finish effects [21,53] would establish design guidelines for printed DAWT components, culminating in wind tunnel and field testing of complete DAWT prototypes to validate system-level power gains.

4.10. Limitations of Steady RANS

The present simulations assume steady flow. Near stall ($\alpha \geq 15^\circ$) and in the post-stall regime, unsteady vortex shedding may occur, which steady RANS cannot resolve. The persistent residual oscillations for the k-ω SST model suggest physical unsteadiness even at $\alpha = 10^\circ$ for this model. Future work should employ URANS or LES for post-stall conditions and to capture dynamic stall phenomena.

Additionally, the results are geometry-specific. The validated model rankings (γ-Re_θ > k-ω SST > XFOIL) are expected to generalize to similar high-camber low-Re airfoils, but quantitative error magnitudes may differ.

5. Conclusions

Based on the comprehensive validation metrics and sensitivity studies presented in this work, the following conclusions are drawn regarding the predictive capabilities of three models (γ-Re_θ, k-ω SST, XFOIL) for low-Reynolds-number flows over a high-camber airfoil, with specific implications for diffuser-augmented wind turbine (DAWT) design.

- Transitional modeling is essential for low-Re aerodynamics. The γ-Re_θ model consistently outperformed both fully turbulent (k-ω SST) and empirical (XFOIL) approaches across all tested conditions (Re = 68k–159k, α = 0–17.5°), achieving the lowest MAPE for lift and drag, near-zero bias, and $R^2 > 0.99$. Its ability to capture LSB dynamics—including the pressure plateau at mid-chord and LSB shrinkage with increasing Re—explains its superior fidelity.
- Fully turbulent assumptions introduce systematic, Re-dependent errors. At Re = 68k, k-ω SST overpredicted CL_max by 9.8% and underpredicted drag by up to 66% due to the elimination of the LSB and artificial delay of separation. Performance improved at Re = 159k as the flow approached fully turbulent conditions, but systematic bias persisted.
- Empirical transition criteria lack generalization. XFOIL's e^n criterion, calibrated for simple pressure gradients, failed at Re = 68k on the high-camber airfoil. Performance converged only at Re = 159k, highlighting the limitation of integral methods with fixed correlations for complex LSB dynamics.

- Pressure distributions expose model deficiencies invisible to integrated forces. At the leading edge, k-ω SST exhibited a large positive bias due to overpredicted suction. At mid-chord, γ-Re_θ uniquely captured the LSB pressure region. In the aft region, γ-Re_θ's negative bias correctly captured reduced pressure recovery, while k-ω SST's bias increased with Re, revealing persistent transitional characteristics even at Re = 159k.
- The γ-Re_θ model demonstrates dual insensitivity to Re and α, a critical property for DAWT design. Its mean lift sensitivity of -0.0049 confirms that accuracy does not degrade with increasing α, while near-zero Re sensitivity ensures robust performance across variable wind speeds. This dual insensitivity eliminates the need for angle-dependent safety factors or operating-point calibration, enabling robust DAWT optimization across the full envelope.
- The custom E423-derived airfoil exhibits gradual stall progression beginning at 15°, making it suitable for DAWT applications where stable power output across variable wind speeds is desirable. Gradual stall avoids abrupt performance collapse, reducing structural loads and control system demands.
- Practical modeling guidelines emerge. γ-Re_θ is recommended for final design validation of DAWT diffusers. XFOIL is viable only at Re = 159k for preliminary trends. k-ω SST requires caution and safety factors near stall, particularly at Re = 68k, where its positive lift bias could lead to under-designed rotors.
- Limitations and future work. Steady RANS cannot capture unsteady vortex shedding in the post-stall regime, which may require scale-resolving simulations or experimental validation for extreme wind events.

Supplementary Materials: The following supporting information can be downloaded at: https://www.mdpi.com/article/10.3390/wind6020028/s1, Highlights, minimal dataset: Table S1: Raw dataset of CL, CD, and Cp used to analyze the results.

Author Contributions: Conceptualization, A.B.D. and V.R.A.; methodology, A.B.D. and V.R.A.; software, A.B.D.; validation, A.B.D., V.R.A. and M.B.K.; formal analysis, A.B.D.; investigation, A.B.D.; resources, A.B.D. and V.R.A.; data curation, A.B.D. and V.R.A.; writing—original draft preparation, A.B.D.; writing—review and editing, A.B.D., V.R.A. and M.B.K.; visualization, A.B.D. and V.R.A.; supervision, V.R.A. and M.B.K.; project administration, A.B.D. and V.R.A.; funding acquisition, A.B.D., V.R.A. and M.B.K. All authors have read and agreed to the published version of the manuscript.

Funding: This research received no external funding.

Institutional Review Board Statement: Not applicable.

Informed Consent Statement: Not applicable.

Data Availability Statement: The original contributions presented in this study are included in the minimal dataset. Further inquiries can be directed to the corresponding authors.

Acknowledgments: The authors gratefully acknowledge Adama Science and Technology University (ASTU), College of Mechanical, Chemical and Material Engineering, Department of Mechanical Engineering, for providing the laboratory facilities and infrastructure that made this research possible. Special thanks go to Sintayhu Shifraw Desta [ASTU, College of Mechanical, Chemical and Material Engineering, Department of Mechanical Engineering, Thermal Laboratory] for his invaluable support during the wind tunnel data collection. The authors also thank the University of Rostock, Rostock, Germany, for covering the article processing charges (APC) through the Excellence in Science and Technology (ExiST) project partnership agreement with Jimma University. During the preparation of this work, the authors used DeepSeek- V4-Pro for language polishing and tone adjustment, including rephrasing sentences to achieve clear expressions. After using the tool, the authors thoroughly reviewed, edited, and approved all content and take full responsibility for the final publication.

Conflicts of Interest: The authors declare no conflicts of interest.

Abbreviations

The following abbreviations are used in this manuscript:

DAWT	Diffuser-Augmented Wind Turbine
RSM	Response Surface Method
RANS	Reynolds Averaged Navier–Stokes
LES	Large Eddy Simulation
DES	Direct Eddy Simulation
Cp	Pressure Coefficient
CL	Lift Coefficient
CD	Drag Coefficient
R^2	Coefficient of Determination
r	Pearson Coefficient
MAE	Mean Absolute Error
MAPE	Mean Absolute Percent Error
RMSE	Root-Mean-Square Error
RE	Relative Error
k	Thousands ('000')
LSB	Laminar Separation Bubble
CL_max	Maximum Lift Coefficient
Re	Reynolds Number
AoA/α	Angle of Attack
TSR	Tip-speed Ratio
CFD	Computational Fluid Dynamics
PE	Percent Error
RSS	Root Sum Square
WLT	Wind-Lens Technology
L	Diffuser Length
D	Throat Domain

Appendix A

Detailed percentage errors in lift and drag predictions across test Re.

Table A1. Percentage errors at Re = 68k.

Model	Coeff.	0°	5°	7.5°	10°	12.5°	15°	17.5°
XFOIL	CL	−11.06	−15.26	−17.14	−12.17	−8.58	−10.96	−5.38
	CD	+99.02	+52.62	+33.33	+14.31	−5.41	−23.12	−26.19
k-ω SST	CL	−7.20	−2.16	+1.34	−1.14	+2.25	+4.78	+10.87
	CD	−44.51	−66.05	−52.84	−44.23	−46.46	−45.80	−36.42
γ-Re_θ	CL	−4.76	−5.01	−4.87	−3.88	−2.12	−2.72	+0.56
	CD	+20.78	+2.58	−0.62	−4.58	−10.93	−16.10	−15.15

Table A2. Percentage errors at Re = 118k.

Model	Coeff.	0°	5°	7.5°	10°	12.5°	15°	17.5°
XFOIL	CL	−7.12	+5.68	+3.49	+1.07	+0.08	+2.51	+11.32
	CD	−28.80	−37.10	−41.40	−42.88	−44.53	−32.73	−27.00
k-ω SST	CL	−10.22	+4.55	+0.74	−5.31	−5.35	−5.00	+1.64
	CD	−29.11	−31.86	−31.82	−26.00	−24.68	−10.39	−6.03
γ-Re_θ	CL	−4.18	+2.61	+1.19	−0.74	−1.05	−0.25	+3.72
	CD	−14.56	−17.45	−18.74	−18.00	−18.28	−11.92	−9.29

Table A3. Percentage errors at Re = 159k.

Model	Coeff.	0°	5°	7.5°	10°	12.5°	15°	17.5°
XFOIL	CL	+2.38	+2.59	−0.82	+0.92	+2.67	+8.38	+9.00
	CD	−26.61	−41.23	−40.65	−41.09	−44.27	−39.64	−29.75
k-ω SST	CL	−8.96	−1.63	−3.70	−4.77	−1.53	+5.03	+5.56
	CD	−6.90	−9.99	−21.66	−24.00	−29.00	−10.14	−1.94
γ-Re_θ	CL	−1.07	+0.45	−0.99	−0.68	+0.50	+3.52	+3.81
	CD	−9.28	−14.35	−16.47	−17.18	−19.13	−13.91	−9.32

Appendix B

Complete pressure coefficient (Cp) distributions for all three Reynolds numbers at selected angles of attack, complementing the force coefficient comparisons shown in Figures 10–12.

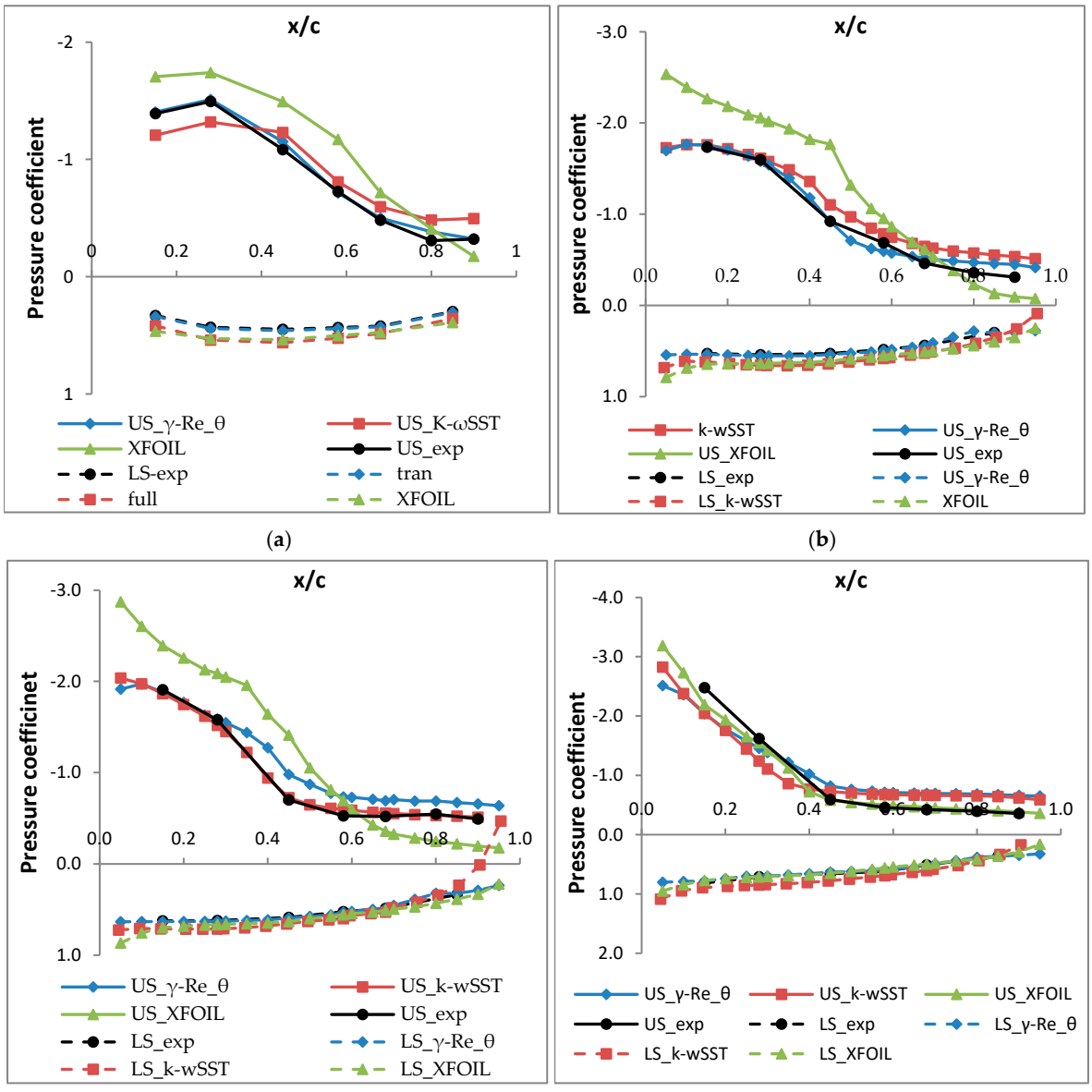

Figure A1. Pressure coefficient distribution at Re = 118k: (**a**) α = 5°, (**b**) α = 10°, (**c**) α = 12.5°, (**d**) α = 17.5°.

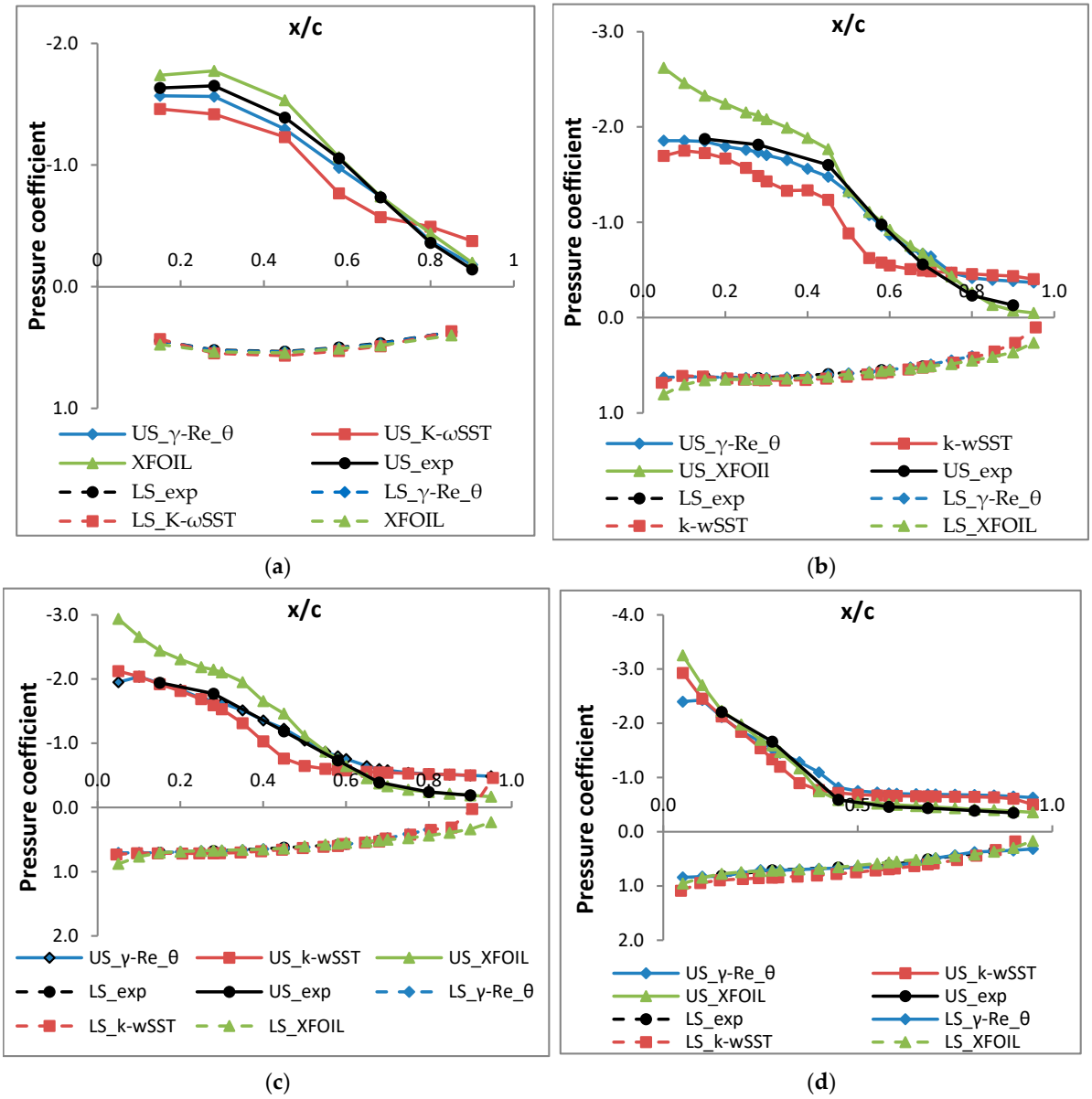

Figure A2. Pressure coefficient distribution at Re = 159k: (**a**) α = 5°, (**b**) α = 10°, (**c**) α = 12.5°, (**d**) α = 17.5°.

Appendix C

Complete angle-resolved mean absolute error (MAE) for pressure coefficient predictions at Reynolds numbers of 68k and 159k and angles of attack (0–17.5°).

Table A4. Angle-Resolved Mean Absolute Error (MAE) for Pressure Coefficient Predictions at Re = 68k.

Re	AoA	XFOIL		k-ω SST		γ-Re_θ	
		Upper	Lower	Upper	Lower	Upper	Lower
68k	5°	0.1687	0.0948	0.1361	0.1417	0.0828	0.0190
	10°	0.1909	0.1065	0.1504	0.1612	0.0952	0.0202
	12.5°	0.1795	0.1126	0.1549	0.1774	0.0948	0.0221
	17.5°	0.1835	0.1683	0.1770	0.2668	0.1175	0.0271

Table A5. Angle-Resolved Mean Absolute Error (MAE) for Pressure Coefficient Predictions at Re = 159k.

Re	AoA	XFOIL	k-ω SST	γ-Re_θ	Re	AoA	XFOIL
159k	5°	0.1063	0.0339	0.1525	0.0499	0.0959	0.0130
	10°	0.1351	0.0382	0.1614	0.0530	0.1042	0.0124
	12.5°	0.1451	0.0381	0.1646	0.0584	0.1068	0.0135
	17.5°	0.1482	0.0535	0.1690	0.0710	0.1103	0.0150

Appendix D

Absolute error of pressure coefficient predictions at all chord positions (x/c) for XFOIL, k-ω SST, and γ-Re_θ models at Re = 68k, 118k, and 159k.

Table A6. Cp prediction errors at Re = 68k.

Re	x/c	XFOIL		k-ω SST		γ-Re_θ	
		Upper	Lower	Upper	Lower	Upper	Lower
68k	0.15	−0.0174	0.0885	0.0113	0.1396	0.0172	0.0183
	0.28	−0.0387	0.0999	0.0379	0.1499	0.0321	0.0172
	0.45	−0.0584	0.1120	0.1057	0.1673	0.0310	0.0199
	0.58	−0.0100	0.1205	0.1256	0.1708	−0.0213	0.0198
	0.68	0.0098	0.1178	0.0665	0.1699	−0.0463	0.0200
	0.80	0.0577	—	0.0125	—	−0.0693	—
	0.85	—	0.1095	—	0.1640	—	0.0189
	0.90	0.0740	—	−0.0059	—	−0.0740	—

Table A7. Cp predictions errors at Re = 118k.

Re	x/c	XFOIL		k-ω SST		γ-Re_θ	
		Upper	Lower	Upper			Upper
118k	0.15	0.0552	0.0471	0.1435	0.0983	0.0156	0.0049
	0.28	0.0134	0.0615	0.1074	0.1037	−0.0068	0.0042
	0.45	−0.0520	0.0686	0.0843	0.1042	−0.0548	0.0034
	0.58	−0.0583	0.0693	0.0235	0.1067	−0.0833	0.0028
	0.68	−0.0440	0.0718	−0.0425	0.1090	−0.1057	0.0023
	0.80	−0.0358	—	−0.1137	—	−0.1446	—
	0.85	—	0.0640	—	0.1040	—	0.0016
	0.90	−0.0352	—	−0.1320	—	−0.1525	—

Table A8. Cp predictions errors at Re = 159k.

Re	x/c	XFOIL		k-ω SST		γ-Re_θ	
		Upper	Lower	Upper			Upper
159k	0.15	−0.1944	0.0152	0.1448	0.0365	0.0189	−0.0008
	0.28	−0.1715	0.0171	0.1842	0.0395	0.0148	−0.0004
	0.45	−0.1301	0.0161	0.1027	0.0424	−0.0579	0.0002
	0.58	−0.0499	0.0166	0.0169	0.0436	−0.1121	0.0006
	0.68	−0.0295	0.0169	−0.0636	0.0442	−0.1596	0.0010
	0.80	0.0078	—	−0.1644	—	−0.1893	—
	0.85	—	0.0126	—	0.0400	—	0.0013
	0.90	0.0139	—	−0.1915	—	−0.1966	—

References

1. Sadorsky, P. Wind energy for sustainable development: Driving factors and future outlook. *J. Clean. Prod.* **2021**, *289*, 125779. [CrossRef]
2. Faisal, A.E.; Lim, C.W.; Al-Quraishi, B.A.J.; Alkawsi, G.; Tan, C.H.; Milano, J.; Phing, C.C.; Al-Farhany, K.; Tiong, S.K. Investigating the techniques used for improving the aerodynamic performance of Archimedes spiral wind turbines: A comprehensive review and future work avenues. *Results Eng.* **2025**, *25*, 103992. [CrossRef]
3. Agha, A.; Chaudhry, H.N. State-of-the-art in development of diffuser augmented wind turbines (DAWT) for sustainable buildings. *Int. J. Renew. Energy Res.* **2018**, *8*, 1369–1385. [CrossRef]
4. Bakare, A.; Patil, N.; Shastri, D. Review of Diffuser Augmented Wind Turbines and development of it in Urban areas. *J. Sci. Adv.* **2025**, *2*, 13–30. [CrossRef]
5. Bontempo, R.; Di Marzo, E.M.; Manna, M. Diffuser augmented wind turbines: A critical analysis of the design practice based on the ducting of an existing open rotor. *J. Wind. Eng. Ind. Aerodyn.* **2023**, *238*, 105428. [CrossRef]
6. Hjort, S.; Larsen, H. Rotor Design for Diffuser Augmented Wind Turbines. *Energies* **2015**, *8*, 10736–10774. [CrossRef]
7. Göltenbott, U.; Ohya, Y.; Yoshida, S.; Jamieson, P. Aerodynamic interaction of diffuser augmented wind turbines in multi-rotor systems. *Renew. Energy* **2017**, *112*, 25–34. [CrossRef]
8. Bontempo, R.; Manna, M. Diffuser augmented wind turbines: Review and assessment of theoretical models. *Appl. Energy* **2020**, *280*, 115867. [CrossRef]
9. Bontempo, R.; Manna, M. Performance analysis of diffuser-augmented wind turbines through a CFD-based actuator disk method coupled with a Blade-Element approach. *Energy Convers. Manag.* **2025**, *342*, 120024. [CrossRef]
10. Nobre, J.C.A.; Andrade, S.C.P.; Sousa, D.L.P.; Guimaraes, T.; Vale, S.B.; Vaz, J.R.P. Performance analysis of diffuser-augmented wind turbines with swept blades using a novel BEMT model. *Glob. Energy Interconnect.* **2026**, *9*, 405–418. [CrossRef]
11. Watanabe, S.; Göltenbott, U.; Ohya, Y.; Yoshida, S. CFD simulation of a multi-rotor system using diffuser augmented wind turbines by lattice Boltzmann method. *J. Phys. Conf. Ser.* **2024**, *2767*, 072002. [CrossRef]
12. Al-Quraishi, B.A.J.; Asmuin, N.Z.; Mohd, S.; Al-wahid, W.A.; Mohammed, A.N.; Didane, D.H. Review on Diffuser Augmented Wind Turbine (DAWT). *Int. J. Integr. Eng.* **2019**, *11*, 178–206. [CrossRef]
13. Shen, X.; Avital, E.; Paul, G.; Rezaienia, M.A.; Wen, P.; Korakianitis, T. Experimental study of surface curvature effects on aerodynamic performance of a low Reynolds number airfoil for use in small wind turbines. *J. Renew. Sustain. Energy* **2016**, *8*, 053303. [CrossRef]
14. Larabi, A.; Pereira, M.; Ravelet, F.; Azzam, T.; Ait-Ali, T.; Oualli, H.; Bakir, F. Experimental and Numerical study on Aerodynamics of Aerofoils at Low Reynolds Number Controlled by Off-Surface Micro-Vortex Generators. In Proceedings of the 25th France Congress of Mechanics, Nantes, France, 2 September 2022.
15. Aziz, M.A.; Gaheen, O.A.; Benini, E.; Elsayed, A.M. Experimental investigation of multi-step airfoils in low Reynolds numbers applications. *Heliyon* **2024**, *10*, e32919. [CrossRef] [PubMed]
16. Rogowski, K.; Mikkelsen, R.F.; Michna, J.; Wiśniewski, J. Aerodynamic performance analysis of NACA 0018 airfoil at low Reynolds numbers in a low-turbulence wind tunnel. *Adv. Sci. Technol. Res. J.* **2025**, *19*, 136–150. [CrossRef]
17. Durmuş, S.; Ulutaş, A. Numerical analysis of NACA 6409 and Eppler 423 airfoils. *Politek. Derg.* **2021**, *26*, 39–47. [CrossRef]
18. Ochi, S.; Kai, S.; Takase, K.; Soneda, K.; Imamura, T.; Rinoie, K.; Yokozeki, T. Aeroelastic Simulation and Experimental Validation of a 3D-Printed Passive Morphing Airfoil. *AIAA J.* **2024**, *62*, 2538–2547. [CrossRef]
19. Olasek, K.; Karczewski, M.; Lipian, M.; Wiklak, P.; Jozwik, K. Wind tunnel experimental investigations of a diffuser augmented wind turbine model. *Int. J. Numer. Methods Heat Fluid Flow* **2016**, *26*, 2033–2047. [CrossRef]
20. Karthikeyan, N.; Kalidasa Murugavel, K.; Arun Kumar, S.; Rajakumar, S. Review of aerodynamic developments on small horizontal axis wind turbine blade. *Renew. Sustain. Energy Rev.* **2015**, *42*, 801–822. [CrossRef]
21. Setlak, L.; Kowalik, R.; Lusiak, T. Aerodynamic Testing of a 3D-Printed Aircraft Model with a Post-Processed Surface. *Materials* **2025**, *18*, 3996. [CrossRef] [PubMed]
22. Jia, S.; Zhang, Z.; Zhang, H.; Song, C.; Yang, C. Wind Tunnel Tests of 3D-Printed Variable Camber Morphing Wing. *Aerospace* **2022**, *9*, 699. [CrossRef]
23. Leloudas, S.N.; Lygidakis, G.N.; Eskantar, A.I.; Nikolos, I.K. A robust methodology for the design optimization of diffuser augmented wind turbine shrouds. *Renew. Energy* **2020**, *150*, 722–742. [CrossRef]
24. Cheung, B.; Arce-Borkent, A.; Wong, J.G. Experiential learning with a 3D printed wind tunnel. *Int. J. Mech. Eng. Educ.* **2026**, 1–14. Available online: https://journals.sagepub.com/doi/pdf/10.1177/03064190261419856 (accessed on 2 June 2026). [CrossRef]
25. Xia, T.; Dong, H.; Yang, L.; Liu, S.; Jin, Z. Investigation on flow structure and aerodynamic characteristics over an airfoil at low Reynolds number—A review. *AIP Adv.* **2021**, *11*, 050701. [CrossRef]
26. Winslow, J.; Otsuka, H.; Govindarajan, B.; Chopra, I. Basic Understanding of Airfoil Characteristics at Low Reynolds Numbers (10^4–10^5). *J. Aircr.* **2018**, *55*, 1050–1061. [CrossRef]

27. Zilstra, A.; Johnson, D.A. Transient Development of a Laminar Separation Bubble Over a Low Reynolds Number Airfoil. *J. Fluids Eng.* **2026**, *148*, 041303. [CrossRef]
28. Wang, M.; Yang, C.; Li, Z.; Zhao, S.; Zhang, Y.; Lu, X. Effects of surface roughness on the aerodynamic performance of a high subsonic compressor airfoil at low Reynolds number. *Chin. J. Aeronaut.* **2021**, *34*, 71–81. [CrossRef]
29. Sunada, S.; Sakaguchi, A.; Kawachi, K. Airfoil Section Characteristics at a Low Reynolds Number. *J. Fluids Eng.* **1997**, *119*, 129–135. [CrossRef]
30. Ayvazoğlu, M.; Keskin, S.; Şahin, R.; Sincar, M.; Sezer, E.A.; Açikel, H.H.; Özden, M.; Genç, M.S. Numerical and Experimental Investigation of Thickness Effect on the Cambered Airfoils at Low Reynolds Numbers. *J. Aeronaut. Space Technol.* **2024**, *17*, 116–134.
31. Bakhtian, N.M.; Babinsky, H.; Thomas, A.L.R.; Taylor, G.K. The low Reynolds number aerodynamics of leading edge flaps. In *45th AIAA Aerospace Sciences Meeting and Exhibit*; AIAA: Reston, VA, USA, 2007. [CrossRef]
32. Ujjin, R.; Ngaongam, C.; Chaikaindee, S.; Boonyanetra, P. 3D-Printed Airfoil Wind Tunnel Aerodynamic Testing and Simulation. In *RSU International Research Conference*; Rangsit University: Bangkok, Thailand, 2019; pp. 929–940.
33. Dogru, S.; Yilmaz, O. Extensive design and aerodynamic performance investigation of diffuser augmented wind turbine (DAWT) guided by generalized actuator disc theory. *Renew. Sustain. Energy Rev.* **2024**, *192*, 114212. [CrossRef]
34. Selig, M.S.; Guglielmo, J.J. High-Lift Low Reynolds Number Airfoil Design. *J. Aircr.* **1997**, *34*, 72–79. [CrossRef]
35. Kassa, B.Y.; Baheta, A.T.; Beyene, A. Aerodynamic performance characteristics of low Re airfoils: A parametric and multi criteria decision study. *Results Eng.* **2024**, *24*, 103174. [CrossRef]
36. Jami, R.; Johnson, D.A. Validation of a RANS Turbulence Model for a S833 Wind Turbine Airfoil With a Trailing Edge Flap Using Oil Visualization and Pressure Taps. *J. Fluids Eng.* **2024**, *146*, 081206. [CrossRef]
37. Ohya, Y.; Karasudani, T. A shrouded wind turbine generating high output power with wind-lens technology. *Energies* **2010**, *3*, 634–649. [CrossRef]
38. Abe, K.; Ohya, Y. An investigation of flow fields around flanged diffusers using CFD. *J. Wind. Eng. Ind. Aerodyn.* **2004**, *92*, 315–330. [CrossRef]
39. Ohya, Y.; Karasudani, T.; Sakurai, A.; Inoue, M. Development of a high-performance wind turbine equipped with a brimmed diffuser shroud. *Trans. Jpn. Soc. Aeronaut. Space Sci.* **2006**, *49*, 18–24. [CrossRef]
40. Demie, A.B.; Ancha, V.R.; Kahsay, M.B. Enhancing Diffuser Augmented Wind Turbine Performance: Aerodynamic Optimization of Diffuser's Cross-section via CFD and Response Surface Methodology. *Results Eng.* **2026**, *30*, 110539. [CrossRef]
41. Paranjape, A.D.; Bajaj, A.S.; Palanganda, S.T.; Parikh, R.; Nayak, R.; Radhakrishnan, J. Computational analysis of high-lift-generating airfoils for diffuser-augmented wind turbines. *Wind. Energy Sci.* **2021**, *6*, 149–156. [CrossRef]
42. Oliveira, T.D.; Tofaneli, L.A.; Santos, A.A.B. Aerodynamic optimization of small diffuser Augmented Wind Turbines: A differential evolution approach. *Energy Convers. Manag. X* **2025**, *26*, 100891. [CrossRef]
43. Zarzoor, A.K.; Jaber, A.A.; Shandookh, A.A. 3D Printing for wind turbine blade manufacturing: A review of materials, design optimization, and challenges. *Eng. Technol. J.* **2024**, *42*, 895–911. [CrossRef]
44. Oberkampf, W.L.; Trucano, T.G. Verification and validation in computational fluid dynamics. *Prog. Aerosp. Sci.* **2002**, *38*, 209–272. [CrossRef]
45. Taylor, N.J.; Rumsey, C.L. CFD Validation Experiments: Toward a Broader Perspective. In *AIAA Scitech 2021 Forum*; AIAA: Reston, VA, USA, 2021. [CrossRef]
46. Wilberforce, T.; Alaswad, A. Performance analysis of a vertical axis wind turbine using computational fluid dynamics. *Energy* **2023**, *276*, 125892. [CrossRef]
47. Atef, M. Numerical Investigation of Transition Turbulence Model for Turbine Airfoil at Low Reynolds Number. In Proceedings of the International Conference on Mechanical, Automotive and Mechatronics Engineering, Dubai, United Arab Emirates, 29–30 April 2023. [CrossRef]
48. Ali, I.; Hussain, T.; Unar, I.N.; Kumar, L.; Ahad, I.U. Turbulence model study for aerodynamic analysis of the leading edge tubercle wing for low-Re. *Heliyon* **2024**, *10*, e32148. [CrossRef]
49. Aftab, S.M.A.; Mohd Rafie, A.S.; Razak, N.A.; Ahmad, K.A. Turbulence Model Selection for Low Reynolds Number Flows. *PLoS ONE* **2016**, *11*, e0153755. [CrossRef]
50. Yu, G.H.; Zhu, X.C.; Du, Z.H. Numerical simulation of a wind turbine airfoil: Dynamic stall and comparison with experiments. *Proc. Inst. Mech. Eng. Part A J. Power Energy* **2010**, *224*, 657–666. [CrossRef]
51. Sun, W. Assessment of advanced RANS turbulence models for prediction of complex flows in compressors. *Chin. J. Aeronaut.* **2023**, *36*, 162–177. [CrossRef]
52. Muhammed, M.; Virk, M.S. On the Fidelity of RANS-Based Turbulence Models in Modeling the Laminar Separation Bubble and Ice-Induced Separation Bubble at Low Reynolds Numbers on Unmanned Aerial Vehicle Airfoil. *Drones* **2024**, *8*, 148. [CrossRef]
53. Zhu, W. Models for wind tunnel tests based on additive manufacturing technology. *Prog. Aerosp. Sci.* **2019**, *110*, 100551. [CrossRef]

54. Rodriguez, C.V.; Celis, C. Design optimization methodology of small horizontal axis wind turbine blades using a hybrid CFD/BEM/GA approach. *J. Braz. Soc. Mech. Sci. Eng.* **2022**, *44*, 254. [CrossRef]
55. Arivalagan, S.; Sappani, R.; Cep, R.; Kumar, M.S. Optimization and Experimental Investigation of 3D Printed Micro Wind Turbine Blade Made of PLA Material. *Materials* **2023**, *16*, 2508. [CrossRef] [PubMed]
56. Chung, H.S.; Kim, S.P.; Choi, Y. Using additive manufactured parametric models for wind tunnel test-based aerodynamic shape optimization. *Rapid Prototyp. J.* **2021**, *27*, 131–144. [CrossRef]
57. Menter, F.R. Two-Equation Eddy-Viscosity Turbulence Models for Engineering Applications. *AIAA J.* **1994**, *32*, 1598–1605. [CrossRef]
58. Rogowski, K.; Krolak, G.; Bangga, G. Numerical Study on the Aerodynamic Characteristics of the NACA 0018 Airfoil at Low Reynolds Number for Darrieus Wind Turbines Using the Transition SST Model. *Processes* **2021**, *9*, 477. [CrossRef]
59. Giacomini, E.; Westerberg, L.G. CFD Analysis of Transition Models for Low-Reynolds Number Aerodynamics. *Appl. Sci.* **2025**, *15*, 10299. [CrossRef]
60. Catalano, P.; de Rosa, D.; D'Alessandro, V.; Marouf, A.; Hoarau, Y.; Miozzi, M.; Righi, M. Modelling laminar separation bubbles at low Reynolds number. In *AIAA SciTech 2024 Forum*; AIAA: Reston, VA, USA, 2024. [CrossRef]
61. Drela, M. XFOIL: An analysis and design system for low Reynolds number airfoils. In *MIT Department of Aeronautics and Astronautics*; Springer: Berlin/Heidelberg, Germany, 1989.
62. GUNT Hamburg. *HM 170 Wind Tunnel—Technical Description and Operating Instructions*; GUNT Hamburg: Barsbüttel, Germany, 2020.
63. Arunvinthan, S.; Pillai, S.N.; Cao, S. Aerodynamic characteristics of variously modified leading-edge protuberanced (LEP) wind turbine blades under various turbulent intensities. *J. Wind. Eng. Ind. Aerodyn.* **2020**, *202*, 104188. [CrossRef]
64. Szwedziak, K.; Łusiak, T.; Bąbel, R.; Winiarski, P.; Podsędek, S.; Doležal, P.; Niedbała, G. Wind tunnel experiments on an aircraft model fabricated using a 3D printing technique. *J. Manuf. Mater. Process.* **2022**, *6*, 12. [CrossRef]
65. Dinulović, M.; Perić, M.; Stamenković, D.; Bengin, A.; Adžić, V.; Trninić, M. Aeroelastic Behavior of 3D-Printed Tapered Polylactic Acid Plates Under Subsonic Flow Conditions. *Materials* **2025**, *18*, 1127. [CrossRef]
66. Virginia Tech Department of Mechanical Engineering. *ME4005: Lab 6—Airfoil*; Unpublished work; Virginia Polytechnic Institute and State University: Blacksburg, VA, USA, 2023; pp. 1–11.
67. *AIAA S-071A-1999*; Assessment of Experimental Uncertainty with Application to Wind Tunnel Testing. AIAA: Reston, VA, USA, 1999. [CrossRef]
68. Moffat, R.J. Contributions to the theory of single-sample uncertainty analysis. *J. Fluids Eng.* **1982**, *104*, 250–258. [CrossRef]
69. Wright, J.R.; Bogue, R.K. Uncertainty in wind tunnel freestream velocity determination. *AIAA J.* **1994**, *32*, 1505–1507.
70. Scanivalve Corp. *Pressure Measurement Systems: Accuracy and Uncertainty Analysis*; Scanivalve Corp: Liberty Lake, WA, USA, 2019.
71. *ASME PTC 19.1-2018*; Test Uncertainty. ASME: New York, NY, UK, 2018.
72. Ansys, Inc. 6.1. Mesh Topologies. In *Ansys Fluent User's Guide*; Ansys, Inc.: Canonsburg, PA, USA, 2025.
73. Coirier, W.J.; Jorgenson, P.C.C. Simulating three-dimensional aeronautical flows on mixed block-structured/semi-structured/unstructured meshes. *Int. J. Numer. Methods Fluids* **2002**, *40*, 245–255.
74. Roache, P.J. Perspective: A Method for Uniform Reporting of Grid Refinement Studies. *J. Fluids Eng.* **1994**, *116*, 405–413. [CrossRef]
75. Thompson, E.J.B.; Gunasekaran, M. Review analysis on laminar separation bubble at low Reynolds numbers. *J. Phys. Conf. Ser.* **2021**, *2054*, 012005. [CrossRef]
76. Tani, I. Low-Speed Flows Involving Bubble Separations. *Prog. Aerosp. Sci.* **1964**, *5*, 70–103. [CrossRef]
77. Rumsey, C.L.; Spalart, P.R. Turbulence Model Behavior in Low Reynolds Number Regions of Aerodynamic Flowfields. In *Proceedings of the 38th AIAA Fluid Dynamics Conference*; AIAA: Reston, VA, USA, 2008.